Computational Geosciences
https://doi.org/10.1007/s10596-020-09944-7

ORIGINAL PAPER

Finite element modelling of geophysical electromagnetic data with goal-oriented *hr*-adaptivity

Hormoz Jahandari[1] · **Scott MacLachlan**[1] · **Ronald D. Haynes**[1] · **Niall Madden**[2]

Received: 2 December 2018 / Accepted: 7 February 2020

Abstract

Large discontinuities (jumps) in coefficients often appear when modelling physical problems involving inhomogeneous media. An example of this is the geophysical electromagnetic (EM) problem, where these jumps occur at interfaces which separate regions of (high) conductivity contrasts. These interfaces, along with other problem features, such as singular EM sources, motivate the use of adaptive mesh refinement to improve the efficiency of the solution of forward problems. Also, pointwise observations are made in geophysical EM surveys, which motivates the use of goal-oriented mesh adaptivity. In this work, we study the combined application of *h*- and *r*-refinements for the modelling of geophysical EM data. The proposed *hr*-adaptivity algorithm is thoroughly investigated in 1D, and then extended, and numerically validated, in 2D, using simple examples as well as a realistic model with irregular interfaces. In 1D, the steady-state diffusion and Helmholtz equations, which are commonly solved for the EM scalar and vector potentials, respectively [16], constitute the physical partial differential equations (PPDEs). In 2D, the Helmholtz equation is used as the PPDE. Additionally, a real 2D problem with a benchmark model is considered where the transverse electric (TE) mode of Maxwell's equations is used as the PPDE. The *r*-refinements are based on an equidistribution principle and variational methods, for the 1D and 2D cases, respectively, which lead to mesh PDEs (MPDEs). The coupled PPDE and MPDE are solved in an iterative manner to enhance the accuracy of the PPDE solution by improving the equidistribution of a monitor function based on *a posteriori* error estimates. The results, in 1D, with two hierarchical error–based monitor functions and a residual error–based monitor function display the similarity between these functions in terms of the accuracy that could be achieved. In both 1D and 2D, comparisons are made between global and goal-oriented adaptivity which show the advantage of goal-oriented error estimates in gaining higher accuracy at a target, compared to global error estimates. In 2D, the results also demonstrate the higher efficiency of *hr*-adaptivity compared with pure *h*-refinement, in terms of computation time.

Keywords *hr*-refinement · Finite element · Electromagnetics · Mesh adaptivity

1 Introduction

In the numerical solution of PDEs, it is common to use mesh refinement to achieve higher accuracy or to reduce the computational cost. There are three main refinement strategies: *h*-refinement, where the mesh is locally refined or coarsened by adding or removing nodes; *p*-refinement, where the order of the underlying polynomial space is adjusted; and *r*-refinement, where the number of nodes in the mesh is fixed but they are moved or redistributed in order to gain higher numerical accuracy. It is also common to use combinations of these adaptivity techniques [1]. The goal of this study is to investigate combined application of *h*- and *r*-adaptivity for the geophysical electromagnetic (EM) modelling problem. While *h*- and *p*-refinements have been extensively studied for this problem [18, 32, 33, 36–38, 50, 52], *hr*-refinement has not been considered before in the geophysical EM literature. Furthermore, since observations in geophysical EM are made pointwise and local accuracy is desired, we consider goal-oriented adaptivity.

There are two main approaches to the EM modelling problem: the direct EM field approach where the problem is formulated in terms of electric and magnetic fields (**E** and **H**), and the potential method where these fields are

✉ Hormoz Jahandari
h.jahandari@mun.ca

Extended author information available on the last page of the article.

replaced by their representations in terms of the magnetic vector potential and electric scalar potential ($\mathbf{A}$ and ϕ):

$$\mathbf{E} = -i\omega\mathbf{A} - \nabla\phi, \tag{1}$$

$$\nabla \times \mathbf{A} = \mu\mathbf{H}. \tag{2}$$

Here, $\omega = 2\pi\tilde{f}$ is angular frequency where $\tilde{f}$ is the ordinary frequency, i is the imaginary unit, μ is magnetic permeability, and a time-dependence of $e^{i\omega t}$ is assumed [19, 59]. The system of equations arising from the potential method is larger than that from the EM field method, but this larger system is better conditioned and can be more efficiently solved using iterative solvers [29]. For this reason, the model problems that are considered here are chosen based on the potential method.

In low-frequency geophysical applications, $\mathbf{E}$ and $\mathbf{H}$ are related by the following form of Maxwell's equations in the frequency domain:

$$\nabla \times \mathbf{E} = -i\omega\mu_0\mathbf{H} \tag{3}$$

$$\nabla \times \mathbf{H} = \sigma\,\mathbf{E} + \mathbf{J}_p, \tag{4}$$

where σ is conductivity, μ_0 is the permeability of free space, and $\mathbf{J}_p$ is an electric source. Taking the curl of Eq. 3 and substituting in Eq. 4 gives the Helmholtz equation for the electric field

$$\nabla \times \nabla \times \mathbf{E} + i\omega\mu_0\sigma\mathbf{E} = -i\omega\mu_0\mathbf{J}_p. \tag{5}$$

Using Eqs. 1 and 2 and applying the Coulomb gauge, this relation can be rewritten as

$$-\nabla^2\mathbf{A} + i\omega\mu_0\sigma\mathbf{A} + \sigma\mu_0\nabla\phi = \mu_0\mathbf{J}_p. \tag{6}$$

Since there are two unknowns in this relation, an additional equation is required. This second equation is derived by taking the divergence of Ampère's law, Eq. 4, which results in the equation of conservation of charge

$$-\nabla\cdot\sigma\mathbf{E} = \nabla\cdot\mathbf{J}_p. \tag{7}$$

Replacing $\mathbf{E}$ with potentials gives

$$i\omega\nabla\cdot\sigma\mathbf{A} + \nabla\cdot\sigma\nabla\phi = \nabla\cdot\mathbf{J}_p. \tag{8}$$

Commonly, either Eq. 5, in the EM field method [28, 43, 44], or Eqs. 6 and 8, in the potential method [16, 29, 42], are solved numerically, subject to boundary conditions approximating vanishing fields far away from the sources.

In this work, as a preliminary study of *hr*-adaptivity, we consider model problems based on analogues of Eqs. 6 and 8, i.e., the steady-state diffusion equation and the Helmholtz equation

$$-\nabla\cdot(\sigma(\boldsymbol{x})\,\nabla u) = f(\boldsymbol{x}), \tag{9}$$

and

$$-\nabla^2 u + \sigma(\boldsymbol{x})\,u = f(\boldsymbol{x}), \tag{10}$$

respectively, where f represents EM sources, and $\boldsymbol{x} = x$ or $\boldsymbol{x} = (x, y)$ for the 1D and 2D cases, respectively. Although $\mathbf{A}$ and ϕ are complex, u is considered real-valued in Eqs. 9 and 10, for simplicity. While in 2D, f represents singular source terms, in 1D, typical singular EM sources are simulated by Gaussian sources. (Note that solutions due to 1D singular sources are piecewise linear and do not replicate solutions due to 3D singular sources or the behavior of real-life EM fields.)

We also consider a realistic 2D geophysical problem with complex-valued solution and a singular point source which represents an infinitely long wire parallel to the conductivity strike. For a two-dimensional conductivity distribution where σ is independent of z, the terms that involve $\partial/\partial z$ vanish, which results in the reduction of Eq. 5 to

$$\nabla\cdot\mu_0^{-1}\nabla u - i\omega\sigma(\boldsymbol{x})\,u = f(\boldsymbol{x}), \tag{11}$$

where u represents E_z and $f(\boldsymbol{x}) = i\omega J_z$ is a point source. Note that Eq. 11 is the transverse electric (TE) mode of Maxwell's equations [14] where the components E_z, H_x, and H_y are present. They are related by

$$\frac{\partial E_z}{\partial x} = i\omega\mu_0 H_y, \quad \frac{\partial E_z}{\partial y} = -i\omega\mu_0 H_x, \tag{12}$$

and

$$\frac{\partial H_y}{\partial x} - \frac{\partial H_x}{\partial y} = \mu_0\sigma(\boldsymbol{x})\,E_z. \tag{13}$$

Of the three refinement methods mentioned earlier, *h*-refinement is the most widely used. This method usually starts with a uniform mesh which is then refined or coarsened based on a measure of the solution error. Typically, a threshold is used to identify the elements that require refinement or the nodes to be eliminated. This procedure is thus iterative, and it is continued until a desired accuracy is achieved. *p*-refinement is commonly considered in the context of the FE methods where local polynomials are used to approximate solution inside the elements. In this approach, the mesh is fixed but the order of the polynomials is increased or decreased, locally, based on the solution error. The combination of *h*- and *p*-refinements, i.e., *hp*-refinement, is also common. It is known that, in some cases, this combination may lead to exponential rates of convergence [15, 48, 51, 54].

In contrast, *r*-refinement typically involves the mapping of a uniform grid, T_c, of a computational domain, Ω_c, to a non-uniform grid, T_h, in a physical domain, Ω. The governing (physical) PDEs (PPDEs) are commonly solved in Ω, and the mapping is performed by solving an auxiliary (mesh) PDE (MPDE) posed on Ω_c (or Ω). Here, we consider a standard approach where the MPDE depends on a monitor function, M, which guides the re-location of the nodes of T_h. In general, M is a function of a local error estimate, constructed from standard *a priori* or *a*

posteriori error estimates, or some measure of continuity at element boundaries [10]. The MPDE is designed such that its solution, T_h, equidistributes M, which is likely to reduce the solution error of the PPDEs [26]. While it is possible to solve the PPDE and MPDE simultaneously or alternately, we choose the latter due to its simplicity and the resulting flexibility in choosing the PDE solvers. In practice, the simultaneous method has been employed mainly for 1D problems [26].

It is also common to combine *h*- and *r*-adaptivity techniques [4, 8, 17, 34, 46, 56], in which *r*-refinement is typically applied on an initial mesh which is then *h*-refined, and this procedure is repeated until a desired solution accuracy is reached. The most common *h*-refinement strategy is local refinement and coarsening based on a tolerance (see the references above). Here, in 1D, uniform *h*-refinements are applied on subdomains of Ω, which are then separately *r*-refined. In 2D, we use both uniform and local *h*-refinement strategies.

As indicated above, the efficiency of an *r*-adaptivity scheme depends on the underlying monitor function, which is, itself, dependent on the error estimate used. *A priori* estimates (e.g., based on the arc length or curvature of the solution) are widely used in the context of mesh adaptivity [1, 10, 30]. However, these estimates commonly require a degree of the knowledge of the geometry or physics of the solution which could be unavailable [23, 57]. For practical problems, *a posteriori* estimates are usually used where an approximation to the gradient or Hessian of the solution is reconstructed from the numerical approximation [63–65]. Alternatively, *a posteriori* error estimates can be derived from hierarchical basis representations, measuring the difference between two FE solutions with different orders of accuracy [5, 23, 27, 31]. In this study, a hierarchical error estimate and an FE residual error estimate are used to construct monitor functions which are then compared, using 1D examples.

While global error estimates are intended to give proportional measures of accuracy over the entire domain, in many applications, including geophysical EM modelling, high accuracy is only required at limited observation locations. In such applications, it is common to use a local error estimate which is typically constructed by weighting the global error estimate, or a measure of it, by a function which is derived by solving a dual (adjoint) form of the original PPDE [45, 49]. Such "goal-oriented" error estimates are employed by [3] and [40, 41] for mesh optimization with *hr*- and *r*-refinement, respectively. In geophysical EM, goal-oriented schemes have been implemented for *h*-refinement [32, 33, 50]. In this work, we investigate the application of these weighted error estimates in combination with monitor functions used within *hr*-refinement.

h-refinement techniques, both global or combined with goal orientation, have been successfully implemented and studied for the modelling of geophysical EM data. The (goal-oriented) dual error estimate weighting (DEW) method is employed in [33, 37] and [36] for the 2D magnetotelluric (MT) and 2.5D controlled source EM (CSEM) problems, respectively. An alternative dual weighted residual (DWR) method, proposed in [47], is applied in [32] for 2D MT and 2.5D CSEM problems. An adaptive higher order FE method is studied in [52] for the 3D CSEM problem, and [38, 50] apply the goal-oriented method proposed in [45] for the 3D MT problem. Goal-oriented *hp*-refinement is employed in [18] for 3D MT problem. A self-adaptive, goal-oriented, *hp*-finite element algorithm with exponential convergence was used in [48] for a 2D well logging problem. In this work, we propose a framework for the modelling of CSEM data using a goal-oriented *hr*-refinement procedure. We present examples in 1D and 2D, but all the components of the algorithm can be readily extended to 3D.

In Section 2 of this manuscript, the model problems, error estimates, and the monitor functions are described, and in Section 3, the *hr*-refinement algorithm is detailed and numerical examples are presented.

2 Error estimates and equidistribution

In this section, we first introduce the model problems and error estimates. Then, the equidistribution principle and monitor functions are described and, finally, a goal-oriented strategy is presented where a modification of the original error estimates is used.

2.1 Model problems and error estimates

The variational formulation of the governing equations, Eqs. 9, 10, and 11 lead to weak forms written as

$$a(u, v) = b(v), \quad \forall v \in V, \tag{14}$$

where u is the unknown solution, V is a Hilbert space of functions over a bounded domain $\Omega \subset \mathbb{R}^n$, $n = 1, 2$, $a(\cdot, \cdot)$ is a bilinear form, and $b(\cdot)$ is a linear functional. Therefore, we have

$$a(u, v) = \int_\Omega \sigma \nabla u \cdot \nabla v \, d\boldsymbol{x}, \tag{15}$$

$$a(u, v) = \int_\Omega (\nabla u \cdot \nabla v + \sigma u v) \, d\boldsymbol{x}, \tag{16}$$

and

$$a(u, v) = \int_\Omega \left(\nabla u \cdot \mu_0^{-1} \nabla v + i\omega \sigma u v\right) d\boldsymbol{x}, \tag{17}$$

for Eqs. 9, 10, and 11, respectively, with

$$b(v) = \int_{\Omega} f\, v\, d\boldsymbol{x}. \tag{18}$$

An FE approximation, u_h, of u, for a given mesh T_h, satisfies

$$a(u_h, v_h) = b(v_h), \quad \forall\, v_h \in V_h, \tag{19}$$

where $V_h \subset V$, $u_h \in V_h$ and V_h is a space of continuous piecewise polynomials corresponding to the elements of T_h, which is on the physical domain Ω.

To minimize the error in an approximation to the solution of one of the problems above, first an estimate of this error is required. Since the true error, $e_h = u - u_h$, is generally unavailable, mesh adaptivity strategies commonly rely on *a posteriori* error estimates. Two types of these estimates are considered here: a hierarchical estimate, $z_h = u_h^q - u_h$, based on the assumption that, for a given norm $\|\cdot\|$, an alternative or reconstructed solution, u_h^q, gives a better approximation to u, i.e.,

$$\left\| u_h^q - u \right\| \leqslant \beta \left\| u_h - u \right\|, \tag{20}$$

where $0 \leqslant \beta < 1$ is a constant [23]. In practice, u_h^q usually corresponds to solutions with higher order basis functions or a finer mesh than that used for u_h. In this work, u_h and u_h^q will be solutions with piecewise linear and quadratic basis functions, respectively, on the same mesh, T_h.

The second type is an FE residual-based error estimate, which is only considered in the 1D case here. This error estimate is constructed based on the second derivative of the 1D solution, u_h''. If u_h represents the piecewise linear FE approximation, considering that u_h'' is zero except at nodes of the mesh, the modified residual of Eq. 9 can be defined as

$$r_h = f + \sigma' u_h'. \tag{21}$$

Using the continuum solution to express f, this relation can be rewritten as

$$r_h = -\sigma' u' - \sigma u'' + \sigma' u_h'. \tag{22}$$

However, assuming σ is a piecewise constant function with jumps only at element interfaces, within any element, $\sigma' = 0$. Therefore, away from the nodes, we can formally write $r_h = -\sigma u''$. We then approximate u'' at the interior nodes of the grid by forming the 3-point Lagrange interpolation of u_h and taking its second derivative. Using these nodal values, u'' is approximated inside the elements by linear interpolation. Although this approximation of u'' restores a dependency on the discrete solution, u_h, which has a vanishing second derivative, we see that this dependency is rather indirect and, so, is not expected to result in a sharp estimate.

While the application of the residual-based estimate described above can be extended to 2D, results will show that this error estimate does not replicate the true error, and therefore, it is presented here for the solution of the 1D diffusion problem only. (There are various post-processing techniques to construct accurate residual-based estimates [64, 65], but these approaches often have cost comparable to hierarchical basis estimates.) The hierarchical- and residual-based error estimates, z_h and r_h, respectively, defined here, are used in Section 2.4 to construct monitor functions.

2.2 Equidistribution principle in 1D

As discussed in Section 1, a mesh, T_h, on the 1D physical domain, Ω, is generated by a coordinate transformation of a uniform 1D grid, T_c, on a computational domain, Ω_c, i.e., $x_i = x(\xi_i)$, $i = 1, \ldots, N+1$, where N is the number of elements. If $u = u(x(\xi))$ is the solution to the PPDE on T_h, the equidistribution of a monitor function $M(u, x(\xi))$ over T_h can be expressed as

$$\int_{x_i}^{x_{i+1}} M(u, x(\xi))\, dx = \frac{1}{N}\, \theta, \quad i = 1, \ldots, N, \tag{23}$$

or equivalently

$$\int_{x_1}^{x(\xi_i)} M(u, x(\xi))\, dx = \frac{i-1}{N}\, \theta, \quad i = 1, \ldots, N+1, \tag{24}$$

where $\theta = \int_{x_1}^{x_{N+1}} M(u, x(\xi))\, dx$. The continuous generalization of this relation can be written as

$$\int_{x_1}^{x(\xi)} M(u, x(\xi))\, dx = \frac{\xi - \xi_1}{|\Omega|}\, \theta. \tag{25}$$

Taking the second derivative of Eq. 25 with respect to ξ gives the 1D MPDE,

$$-\frac{d}{d\xi}\left(M(u, x(\xi))\, \frac{dx}{d\xi} \right) = 0. \tag{26}$$

It is common to solve the discretized form of this relation as a nonlinear BVP with Dirichlet boundary conditions using Newton's method [26] or a simple linearization. This MPDE can also be written in terms of the inverse coordinate transformation, $\xi = \xi(x)$, as

$$-\frac{d}{dx}\left(\frac{1}{M(u, x)}\, \frac{d\xi}{dx} \right) = 0, \tag{27}$$

which can be discretized and solved as a linear BVP. Since the solution of this MPDE is in Ω_c, either this solution should be transferred to Ω, where the solution of the PPDE is defined, or the corresponding PPDE should be coordinate transformed and solved for solutions in Ω_c. Note that the discrete solution of the linear MPDE in Eq. 27 is not necessarily equivalent to that of the nonlinear MPDE in Eq. 26. For an equivalent solution at the discrete level, it might be necessary to solve the linear MPDE in an

iterative manner [26]. The nonlinear MPDE is, however, more popular and in this study a fixed-point iteration method applied to the linear FE discretization is used to solve Eq. 26. In 2D, however, we prefer to solve linear MPDEs, as explained in the following section.

2.3 Mesh PDEs in two dimensions

In higher dimensions, it is common to use a variational approach to derive the MPDE. In a 2D variational method, the coordinate transformation, $\boldsymbol{x} = (x(\xi,\eta), y(\xi,\eta))$, is defined as the minimizer of a functional, $\tilde{I}$, which commonly involves a monitor function, and possibly other measures to determine mesh properties. This functional can be formulated in terms of $\boldsymbol{x}$ or its inverse transformation, $\boldsymbol{\xi} = (\xi(\boldsymbol{x}), \eta(\boldsymbol{x}))$. It can be shown that the solution of the linear 1D MPDE in Eq. 27 is the minimizer of the functional,

$$\tilde{I}[\xi] = \frac{1}{2}\int_{\Omega} \frac{1}{M}\left(\frac{\partial \xi}{\partial x}\right)^2 dx, \tag{28}$$

[10]. A generalization of this functional in two dimensions is given by

$$\tilde{I}[\xi,\eta] = \frac{1}{2}\int_{\Omega} \left(\nabla\xi^T \boldsymbol{M}^{-1}\nabla\xi + \nabla\eta^T \boldsymbol{M}^{-1}\nabla\eta\right) d\boldsymbol{x}, \tag{29}$$

where $\nabla = \left(\partial_x, \partial_y\right)^T$ and $\boldsymbol{M}$ is a matrix-valued monitor function [11, 24]. The MPDEs whose solutions minimize the functional in Eq. 29 are

$$\nabla\cdot\left(\boldsymbol{M}^{-1}\nabla\xi\right) = 0, \quad \nabla\cdot\left(\boldsymbol{M}^{-1}\nabla\eta\right) = 0. \tag{30}$$

Since T_h is in Ω, it is usual to write these MPDEs in terms of $\boldsymbol{x}$, and then solve nonlinear BVPs in Ω_c [6, 12, 13, 22, 25, 35, 55, 56, 62]. However, it is also common to solve the equations in Eq. 30 directly, as linear BVPs with appropriate boundary conditions, and then map (coordinate transform) the solutions to Ω in order to calculate the physical mesh [20, 35]. A simpler alternative to this coordinate transformation, which can be as expensive as solving the nonlinear BVPs, is to use bilinear interpolation as an approximation to the transformation between $\boldsymbol{x}$ and $\boldsymbol{\xi}$ [7, 26, 58]. For the 2D examples in Section 3.7, we use the linear MPDEs in Eq. 30 combined with bilinear interpolation. Also, we consider an isotropic mesh adaptation, i.e., $\boldsymbol{M} = MI$, where I is the 2×2 identity matrix and M is a scalar monitor function defined in the following section. This choice of $\boldsymbol{M}$ gives Winslow's variable diffusion mesh generation method [60, 61]. The evaluation of various existing MPDEs and anisotropic monitor functions will be considered in a future study.

2.4 Monitor functions

The hierarchical and FE residual error estimates introduced in Section 2.1 are used to construct three types of piecewise-constant monitor functions, M. In the first type, the hierarchical error estimate, $z_h = u_h^q - u_h$, is directly used to create an error-based monitor function, following a procedure similar to [21]. We first define an elementwise error indicator,

$$\langle z_h\rangle_j = \frac{1}{\left|K_j\right|^2}\int_{K_j} |z_h|^2\, d\boldsymbol{x}, \qquad j = 1,\ldots,N, \tag{31}$$

where K_j is the jth element of T_h, $\left|K_j\right|$ represents the size of K_j, and $d\boldsymbol{x}$ is written for both the 1D and 2D cases. Using Eq. 20 and the triangle inequality gives

$$\begin{aligned}
\|u-u_h\| \leqslant C\left\|u_h^q - u_h\right\| &= C\left(\sum_{j=1}^{N}\int_{K_j}|z_h|^2\, d\boldsymbol{x}\right)^{\frac{1}{2}} \\
&= C\left(\sum_{j=1}^{N}\left|K_j\right|^2\langle z_h\rangle_j\right)^{\frac{1}{2}} \\
&\leqslant C\left(\sum_{j=1}^{N}\left|K_j\right|^2\left[\alpha_h + \langle z_h\rangle_j\right]\right)^{\frac{1}{2}} \\
&= C\,\alpha_h^{\frac{1}{2}}\left(\sum_{j=1}^{N}\left|K_j\right|^2\left[1+\frac{1}{\alpha_h}\langle z_h\rangle_j\right]\right)^{\frac{1}{2}},
\end{aligned} \tag{32}$$

where $C = 1/(1-\beta)$, $(0\leqslant\beta<1)$, $\|\cdot\| = \|\cdot\|_2$, and α_h is an arbitrary positive value used for regularization.

Equation 32 gives an upper bound for the hierarchical error estimate. For this upper bound, a lower bound can be derived using Hölder's inequality,

$$\sum_{j=1}^{N}\left|K_j\right|^2\left(1+\frac{1}{\alpha_h}\langle z_h\rangle_j\right) \geqslant \frac{1}{N}\left[\sum_{j=1}^{N}\left|K_j\right|\left(1+\frac{1}{\alpha_h}\langle z_h\rangle_j\right)^{\frac{1}{2}}\right]^2. \tag{33}$$

The minimum value of this lower bound is realized by having equality in this relation, i.e., requiring

$$\left|K_i\right|\left(1+\frac{1}{\alpha_h}\langle z_h\rangle_i\right)^{\frac{1}{2}} = \frac{1}{N}\sum_{j=1}^{N}\left|K_j\right|\left(1+\frac{1}{\alpha_h}\langle z_h\rangle_j\right)^{\frac{1}{2}}, \tag{34}$$

where $i = 1,\ldots,N$. Comparing this relation with the equidistribution principle in Eq. 23 indicates that the hierarchical error–based monitor function can be defined as

$$M_j = \left(1+\frac{1}{\alpha_h}\langle z_h\rangle_j\right)^{\frac{1}{2}}, \qquad j = 1,\ldots,N, \tag{35}$$

where M_j is the value of M on element K_j. To define α_h, which is often called the intensity, or regularization, parameter, the method used by [22] is considered, which

positions approximately 50% of the nodes where $M_j \gg 1$. This is achieved by requiring

$$\sum_{j=1}^{N} |K_j| M_j \leqslant \sum_{j=1}^{N} |K_j| \left(1 + \alpha_h^{-\frac{1}{2}} \langle z_h \rangle_j^{\frac{1}{2}}\right) \leqslant 2\,|\Omega|\,, \quad (36)$$

which can be rewritten as

$$|\Omega| + \alpha_h^{-\frac{1}{2}} \sum_{j=1}^{N} |K_j| \langle z_h \rangle_j^{\frac{1}{2}} \leqslant 2\,|\Omega|\,, \quad (37)$$

where $|\Omega|$ represents the domain size. Note that Eq. 35 and Jensen's inequality are used to obtain the first inequality in Eq. 36. The easiest option to define α_h is to use equality in Eq. 37 which results in

$$\alpha_h = \left(\sum_{j=1}^{N} |K_j| \langle z_h \rangle_j^{\frac{1}{2}}\right)^2 / |\Omega|^2\,. \quad (38)$$

As $\alpha_h \to \infty$, $M_j \to 1$, which results in a uniform mesh as the solution of the MPDE. When $\alpha_h \to 0$, however, the effect of the error indicator increases and the mesh adaptivity intensifies.

The second type of hierarchical error–based monitor function used here is based on the Hessian of this error estimate. For this, we use the anisotropic interpolation error bound derived by [23] which states that $\|u - u_h\| \leqslant C\,\|z_h\|$, where

$$\begin{aligned} C\,\|z_h\| &\geqslant C \sum_{j=1}^{N} \left(|K_j| \left[1 + \frac{1}{\alpha_h} \langle z_h \rangle_j\right]^{\frac{2}{5}}\right)^5 \\ &\geqslant C\,N^{-4} \left(\sum_{j=1}^{N} |K_j| \left[1 + \frac{1}{\alpha_h} \langle z_h \rangle_j\right]^{\frac{2}{5}}\right)^5. \end{aligned} \quad (39)$$

In this relation, again $C = \frac{1}{1-\beta}$, $(0 \leqslant \beta < 1)$, but the error indicator is the second derivative of the hierarchical error estimate, i.e., $\langle z_h \rangle_j = z''_{h,j}$. (We apply this Hessian-based monitor function in 1D only.) We note that $z''_{h,j}$ is a constant on element j, since $z_h = u_h^q - u_h$, and u_h^q and u_h are piecewise quadratic and piecewise linear approximations. Also, note that Hölder's inequality is used to obtain the lower bound of the hierarchical error estimate in Eq. 39. Again, to derive a monitor function, equality in Eq. 39 should be considered which is satisfied if

$$|K_i| \left(1 + \frac{1}{\alpha_h} \langle z_h \rangle_i\right)^{\frac{2}{5}} = \frac{1}{N} \sum_{j=1}^{N} |K_j| \left(1 + \frac{1}{\alpha_h} \langle z_h \rangle_j\right)^{\frac{2}{5}}, \quad (40)$$

where $i = 1, \ldots, N$. Comparing this relation with the equidistribution principle in Eq. 23 indicates that the hierarchical error Hessian-based monitor function can be defined as

$$M_j = \left(1 + \frac{1}{\alpha_h} \langle z_h \rangle_j\right)^{\frac{2}{5}}, \quad j = 1, \ldots, N, \quad (41)$$

where, again, $\langle z_h \rangle_j = z''_{h,j}$. Following [23], the intensity parameter, α_h, is calculated by solving

$$\sum_{j=1}^{N} |K_j| \left(1 + \frac{1}{\alpha_h} \langle z_h \rangle_j\right)^{\frac{2}{5}} = 2\,|\Omega|\,, \quad (42)$$

using a bisection method, subject to the bounds

$$\left[\frac{0.5}{|\Omega|} \sum_{j=1}^{N} |K_j| \langle z_h \rangle_j^{\frac{2}{5}}\right]^{\frac{5}{2}} \leqslant \alpha_h \leqslant \left[\frac{1}{|\Omega|} \sum_{j=1}^{N} |K_j| \langle z_h \rangle_j^{\frac{2}{5}}\right]^{\frac{5}{2}}. \quad (43)$$

In the third type of monitor function, the FE residual error estimate, r_h, is used to form a residual-based monitor function (used here for the diffusion problem and in 1D only). The residual-based monitor function derived in [21] and [26] is used, where

$$M_j = \left(1 + \frac{1}{\alpha_h} \langle r_h \rangle_j^2\right)^{\frac{1}{3}}, \quad j = 1, \ldots, N, \quad (44)$$

with the intensity parameter defined as

$$\alpha_h = \left(\sum_{j} |K_j| \langle r_h \rangle_j^{\frac{2}{3}}\right)^3 / \ |\Omega|^3\,, \quad (45)$$

and the residual error indicator, $\langle r_h \rangle$, is defined as

$$\langle r_h \rangle_j = \left(\frac{1}{|K_j|} \int_{K_j} |r_h|^2\, dx\right)^{\frac{1}{2}}. \quad (46)$$

These monitor functions are compared in Section 3.4.

2.5 Goal-oriented error estimate

In the context of goal-oriented adaptivity, typically the goal is to control the error in a (physically relevant) quantity of interest that is given by a goal functional $g(u)$. Due to the linearity of g, the error of this functional, ε^g, can be written as

$$\varepsilon^g = g(u) - g(u_h) = g(u - u_h) = g(e_h)\,. \quad (47)$$

The aim, therefore, is to derive a local error estimate with respect to $g(e_h)$. If the variational form of the primary PPDE problem is given as $a(u, v) = b(v)$, $\forall\, v \in V$, then $a(v, w) = g(v)$, $\forall\, v \in V$, is an adjoint (dual) of this problem [45], where u and w are the solutions of the primary and dual problems, respectively. If the error in w is given by e_w, we can write

$$g(e_h) = a(e_h, w) = a(e_h, w_h + e_w)\,. \quad (48)$$

Since $a\,(e_h, w_h) = 0$, due to Galerkin orthogonality, we have

$$g\,(e_h) = a\,(e_h, e_w)\,. \tag{49}$$

Also, note that $a\,(e_h, w) = a\,(w, e_h)$, since $a\,(.,.)$ is self-adjoint. Brenner and Scott, Oden and Prudhomme, and Ren et al. [9, 45, 50] use the Cauchy-Schwarz inequality to derive an upper bound for the local error $g\,(e_h)$ as

$$\begin{aligned} |g(e_h)| = |a\,(e_w, e_h)| &\leqslant \sum_{j=1}^{N} \left|a_j\,(e_w, e_h)\right| \\ &\leqslant \sum_{j=1}^{N} \|e_h\|_{e,j}\,\|e_w\|_{e,j} \\ &\cong \sum_{j=1}^{N} C_n\,\|e_h\|_{2,j}\,\|e_w\|_{2,j}\,, \end{aligned} \tag{50}$$

where C_n is a constant that depends on the size of T_h and $\|\cdot\|_{e,j}$, $\|\cdot\|_{2,j}$, and $a_j\,(\cdot,\cdot)$ denote the restrictions of the energy norm, L_2-norm, and the bilinear form to the jth element of T_h, respectively. Therefore, if global hierarchical error estimates for e_h and e_w are given as z_h and z_w, respectively, using Eq. 50, an error estimate for $g\,(e_h)$ can be derived as

$$\left\|z_g\right\|_{2,j} = \|z_h\|_{2,j}\,\|z_w\|_{2,j}\,, \qquad j = 1, \ldots, N. \tag{51}$$

This goal-oriented error estimate, z_g, is then used instead of the global z_h in the construction of any of the three monitor functions defined in the previous section.

Following [45, 50], $g(v)$, which gives a measure of solution at the target and contains the source term of the dual PPDE problem, is given by

$$g\,(v) = \int_{\Omega} f\,(u)\; v\; d\boldsymbol{x}, \tag{52}$$

where $d\boldsymbol{x}$ is written for both the 1D and 2D cases, and the source term is defined as

$$f\,(u) = \sum_{j=1}^{\tilde{N}} \frac{1}{|\tilde{K}_j|} \int_{\tilde{K}_j} u\; d\boldsymbol{x}. \tag{53}$$

In this relation, u is the solution of the primary PPDE problem, $\tilde{K}_j$, $j = 1, \ldots, \tilde{N}$, are the elements inside the target region and $\tilde{N}$ is the number of these elements. In practice, $f\,(u)$ represents singular sources located at the center of the elements inside the target region. Note that to calculate z_w, linear and quadratic solutions of the dual problem with the source terms $f = f\,(u_h)$ and $f = f\left(u_h^q\right)$, respectively, are required, which means that the cost of the calculation of the local error estimate, z_g, is twice that of the global z_h.

3 Numerical examples

In this section, we propose and validate *hr*-adaptivity procedures for the solution of the problems presented in Section 2.1. We compare the effectiveness of the three monitor functions described in Section 2.4 when applied to a selection of 1D test problems, considering the effect of the number of starting elements, N, and the influence of fixing nodes at the interfaces of the regions. Furthermore, the stopping criteria for the *r*-refinement procedure and the effectiveness of the goal-oriented error estimates are investigated. The section concludes with validation of the algorithm by applying it to 2D problems.

3.1 Test problems in 1D

The test problems considered here, corresponding to the 1D version of the diffusion and Helmholtz equations, Eqs. 9 and 10, are

$$\begin{cases} -\left(\sigma\,(x)\,u'\right)' = f\,(x)\,, & x \in (0, 10)\,, \\ u(0) = 0,\;\; u(10) = 0, \end{cases} \tag{54}$$

and

$$\begin{cases} -u'' + \sigma\,(x)\,u = f\,(x)\,, & x \in (0, 10)\,, \\ u(0) = 0,\;\; u(10) = 0, \end{cases} \tag{55}$$

respectively. The physical domain, $\Omega = [0, 10]$, represents a layered halfspace which is schematically shown in Fig. 1. The layers in this model consist of an air layer, $x \in [5, 10]$, a ground layer, $x \in [0, 5]$, and an anomalous layer inside the ground, $x \in [3, 4]$. Therefore, there are interfaces at $x = 3$,

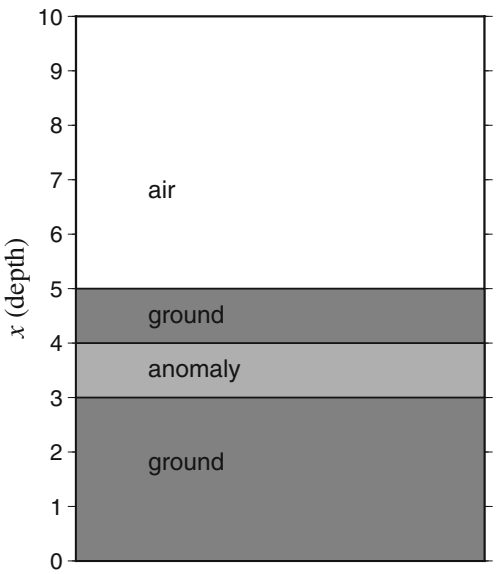

Fig. 1 The layered halfspace model used for the 1D examples. Various coefficient values for these layers are given in Eqs. 56–58

4, and 5. In the following examples, piecewise constant coefficients for these layers, from $x = 0$ to 10, are

$$\begin{cases} \sigma_1 = 10^6, 10^3, 10^6, 1, & (56) \\ \sigma_2 = 10^5, 10^{10}, 10^5, 1, & (57) \\ \sigma_3 = 10^6, 10^2, 10^6, 10^{-6}, & (58) \end{cases}$$

where σ_1 and σ_2 are used for the diffusion problem and σ_3 for the Helmholtz problem. These values are chosen to represent common underground conductivity contrasts, and also to give solution behaviors which necessitate, or at least benefit from, refinement.

The source terms used for the problems in Eqs. 54 and 55 are

$$f(x) = -\frac{8\,c^4\,(x-4)^2}{\left(1+c^2\,(x-4)^2\right)^3} + \frac{2\,c^2}{\left(1+c^2\,(x-4)^2\right)^2}, \quad (59)$$

and

$$f(x) = -\frac{8\,c^4\,(x-4)^2}{\left(1+c^2\,(x-4)^2\right)^3} + \frac{2\,c^2}{\left(1+c^2\,(x-4)^2\right)^2} + \frac{1}{1+c^2\,(x-4)^2}, \quad (60)$$

respectively. The constant c controls the width of these Gaussian-like functions. In the 1D examples that follow, $c = 20$ and $c = 2$ are chosen for the diffusion and Helmholtz problems, respectively. The solution to the test problems with these sources in a wholespace with $\sigma = 1$ is $u(x) = 1/\left(1+c^2\,(x-4)^2\right)$, which simulates solutions with singular sources commonly used in EM modelling problems in higher dimensions.

3.2 *hr*-refinement algorithm

The procedure proposed for the *hr*-refinement of the FE models is described by Algorithms 1–4. Algorithm 1 lays out the main *hr*-adaptivity workflow which uses the procedures in Algorithms 2 and 3 or 4. Algorithm 2 describes the *h*-refinement, and Algorithms 3 and 4 give the procedure for *r*-refinement using the hierarchical and residual error estimates, respectively.

In Algorithm 1, given an initial number of elements, N, and computational and physical domains, Ω_c and Ω, respectively, uniform meshes, T_c and T_h (on Ω_c and Ω, respectively) are created. T_h is then *r*-refined by finding a mapping of T_c which is (approximately) M-uniform, i.e., M is equidistributed among the elements of T_h. This is done by solving an MPDE, from Sections 2.2 and 2.3, as a BVP, using a linear FE method. If the desired accuracy (measured by the L_2-norm of an error estimate) in the solution of the PPDE problem, with this *r*-refined grid, is not reached, an *h*-refinement is performed which is followed by another *r*-refinement and this procedure is continued

Algorithm 1 The main *hr*-refinement procedure.

procedure *hr*-refinement($N, \Omega_c, \Omega, m, \sigma, \tau_p, \tau_h, \tau_r, \tau_e$)
▷ N is the initial number of elements. Ω_c and Ω are the computational and physical domains, respectively. m is the number of regions in Ω_c and Ω. σ is a coefficient function for the PPDE. τ_p is a tolerance for the *r*-refinement. τ_h is a parameter to calculate the number of *h*-refinement steps and τ_r is a limit for this number. E is the of error estimate or the global level of equidistribution and τ_e is a target value for E to be reached by this procedure.
  T_c = uniform-grid (Ω_c, N)
  T_h = uniform-grid (Ω, N)
  ▷ Initially, T_c and T_h are both uniform meshes.
  (T_h, M, E) = *r*-refinement (σ, T_c, T_h, τ_p)
  ▷ *r*-refine T_h and generate a new mesh with the same name.
  while $E > \tau_e$ **do**
    (T_c, T_h, N)=*h*-refinement(Ω_c, Ω, m, T_h, N, M, τ_h, τ_r)
    ▷ *h*-refine T_h and generate a new mesh with the same name.
    (T_h, M, E) = *r*-refinement (σ, T_c, T_h, τ_p)
  end while
end procedure

until the termination criterion is satisfied. If Ω consists of a single region and the MPDE is sufficiently solved, then the global equidistribution is complete in a single iteration of the procedure in Algorithm 1. If there is need for higher accuracy, *h*-refinement is performed by dividing each element of T_h into 2^n elements (where $\Omega \subset \mathbb{R}^n$). (In this way, ideally, the relative equidistribution is preserved). However, in general, Ω consists of multiple regions, i.e., $\Omega = \bigcup_{k=1}^{m} \Omega^{(k)}$ and $\mathrm{T}_h = \bigcup_{k=1}^{m} \mathrm{T}_h^{(k)}$, and we solve the MPDE problem over Ω as m separate MPDE problems for each $\Omega^{(k)}$ (more details in Section 3.3). Also, in this scenario, subsequent to a successful *r*-refinement, M is equidistributed inside each region, i.e., $\theta^{(k)}$ defined by

$$\theta^{(k)} = \int_K M\,d\boldsymbol{x}, \quad \forall K \in \mathrm{T}_h^{(k)}, \quad k = 1, \ldots, m, \quad (61)$$

is a constant. However, it is likely that M is not equidistributed over Ω, and $\theta^{(k)}$ have different values. If there is need for higher accuracy, and hence *h*-refinement, then the global equidistribution of M is improved by *h*-refining those regions which exhibit higher values of $\theta^{(k)}$. This sequence of *h*- and *r*-refinements (explained in more detail in the following paragraphs) is continued until the stopping criterion is satisfied. We should note, however, that in a multi-region scenario the goal is not to reach a

Algorithm 2 *h*-refinement of a given mesh, based on the difference in error values between the regions.

procedure *h*-refinement(Ω_c, Ω, m, T_h, N, M, τ_h, τ_r)
▷ Ω_c and Ω are the computational and physical domains, respectively. m is the number of regions in Ω_c and Ω. T_h and N are the given mesh, in Ω, and its number of elements, respectively. M is the monitor function corresponding to T_h. τ_h is a parameter to calculate the number of *h*-refinement steps and τ_r is a limit for this number. $n = 1$ and 2, for 1D and 2D, respectively.
  $\theta_K \leftarrow \int_K M\,dx,\ \forall K \in \mathrm{T}_h$
  for $k = 1$ to m **do**
    $r = \mathrm{floor}(\log(\max(\theta_K^{(k)})/\min(\theta_K))/\log(\tau_h))$
    $r = \min(r, \tau_r)$
    ▷ The number of times to refine the k^{th} region, based on τ_h and τ_r.
    for $l = 1$ to r **do**
      $\Gamma = h\text{-refine}\ (\mathrm{T}_h^{(k)},\ N^{(k)})$
      $\mathrm{T}_h^{(k)} \leftarrow \Gamma$
      ▷ $\mathrm{T}_h^{(k)}$ is *h*-refined by dividing each of its elements into 2^n elements.
      $N^{(k)} \leftarrow 2^n N^{(k)}$
      ▷ The new number of elements in the k^{th} region.
    end for
    $\mathrm{T}_c^{(k)} = \text{uniform-grid}\left(\Omega_c^{(k)},\ N^{(k)}\right)$
    ▷ Generate a uniform mesh for the k^{th} region of Ω_c.
  end for
  $\mathrm{T}_h \leftarrow \bigcup_{k=1}^{m} \mathrm{T}_h^{(k)}, \quad \mathrm{T}_c \leftarrow \bigcup_{k=1}^{m} \mathrm{T}_c^{(k)}$
  $N \leftarrow \sum_{k=1}^{m} N^{(k)}$
end procedure

Algorithm 3 *r*-refinement of a given mesh. Hierarchical error estimates are used to construct the monitor functions.

procedure *r*-refinement$_1$(m, σ, T_c, T_h, τ_p)
▷ m is the number of regions in Ω_c and Ω, σ is a coefficient function for the PPDE, and T_c and T_h are meshes in Ω_c and Ω, respectively. τ_p is a tolerance for the *r*-refinement procedure.
  $i \leftarrow 1$
  $\mathrm{T}_h^i \leftarrow \mathrm{T}_h$
  $z_h^i \leftarrow 0$
  $P \leftarrow \tau_p + 1$
  while $P > \tau_p$ **do**
    $i \leftarrow i + 1$
    $u_h = \text{FE-linear}\left(\sigma, \mathrm{T}_h^{i-1}\right)$
    $u_h^q = \text{FE-quadratic}\left(\sigma, \mathrm{T}_h^{i-1}\right)$
    ▷ Solve the PPDE using linear and quadratic FE schemes.
    $z_h^i \leftarrow \left|u_h^q - u_h\right|$
    ▷ Form the hierarchical error estimate.
    $P \leftarrow \left(\left\|z_h^i\right\|_2 - \left\|z_h^{i-1}\right\|_2\right) / \left\|z_h^i\right\|_2 \times 100$
    $M = \text{monitor-func}\left(z_h^i, \mathrm{T}_h^{i-1}\right)$
    ▷ Form the monitor function.
    for $k = 1$ to m **do**
      $\mathrm{T}_h^{(k),i} = \text{MPDE-solve}\left(M^{(k)}, \mathrm{T}_h^{(k),i-1}, \mathrm{T}_c^{(k)}\right)$
      ▷ Solve the MPDE for the k^{th} region.
    end for
    $\mathrm{T}_h^i \leftarrow \bigcup_{k=1}^{m} \mathrm{T}_h^{(k),i}$
  end while
  $\mathrm{T}_h \leftarrow \mathrm{T}_h^i$
  $E \leftarrow \left\|z_h^i\right\|_2$
end procedure

global equidistribution but to progress towards it in order to efficiently improve the accuracy.

The *h*-refinement procedure is described by Algorithm 2. The main inputs to this procedure are T_h and the monitor function corresponding to this mesh, M. A tolerance, τ_h, should also be provided which controls the number of *h*-refinement steps required to reduce the difference between the values of $\theta^{(k)}$ for the different regions. The number of *h*-refinements for each region is limited by τ_r. In principle, the ratio between $\max_k \theta^{(k)}$ and $\min_k \theta^{(k)}$ over T_h, and the tolerance τ_h, are used to decide the number of *h*-refinements required for each region (see Algorithm 2 for more details). However, since the equidistribution of M is never exactly achieved, in practice $\theta^{(k)}$ is not a constant, and therefore, for the kth region, the ratio between $\max_{K \in \mathrm{T}_h^{(k)}} \theta_K$ and $\min_{K \in \mathrm{T}_h} \theta_K$ is used, where θ_K is a piecewise constant quantity defined as

$$\theta_K = \int_K M\,d\boldsymbol{x}, \quad \forall K \in \mathrm{T}_h. \tag{62}$$

Any region of the new mesh, $\mathrm{T}_h^{(k)}$, which has been *h*-refined, as described above, should then be *r*-refined. This procedure is described by Algorithms 3 and 4, which only differ in the type of error estimate used and the stopping criterion.

Algorithm 3 uses the hierarchical error estimate where the difference between two solutions with different orders of accuracy, u_h and u_h^q, is used to construct the error estimate, z_h, as described in Section 2.1. This error estimate is then used to form a monitor function, M, which is equidistributed over the elements of each of the regions, $\mathrm{T}_h^{(k)}$, by solving an

Algorithm 4 r-refinement of a given mesh. FE residual-based error estimate is used to construct the monitor function.

procedure r-refinement$_2(m, \sigma, \mathrm{T}_c, \mathrm{T}_h, \tau_p)$
▷ m is the number of regions in Ω_c and Ω, σ is a coefficient function for the PPDE, and T_c and T_h are meshes in Ω_c and Ω, respectively. τ_p is a tolerance for the r-refinement procedure.
  $i \leftarrow 1$
  $\mathrm{T}_h^i \leftarrow \mathrm{T}_h$
  $Q^i \leftarrow 0$
  $P \leftarrow \tau_p + 1$
  while $P > \tau_p$ **do**
    $i \leftarrow i + 1$
    $u_h = \text{FE-linear}\left(\sigma, \mathrm{T}_h^{i-1}\right)$
    ▷ Solve the PPDE using a linear FE scheme.
    $r_h \leftarrow \sigma u_h''$
    ▷ Form the residual-based error estimate.
    $M = \text{monitor-func}\left(r_h, \mathrm{T}_h^{i-1}\right)$
    ▷ Form the monitor function.
    $\theta_K \leftarrow \int_K M\,dx, \ \forall K \in \mathrm{T}_h^{i-1}$
    $Q^i \leftarrow \left(\max_{K\in\mathrm{T}_h} \theta_K - \min_{K\in\mathrm{T}_h} \theta_K\right) / \min_{K\in\mathrm{T}_h} \theta_K \times 100$
    $P \leftarrow \left|Q^i - Q^{i-1}\right| / Q^i \times 100$
    for $k = 1$ to m **do**
      $\mathrm{T}_h^{(k),i} = \text{MPDE-solve}\left(M^{(k)}, \mathrm{T}_h^{(k),i-1}, \mathrm{T}_c^{(k)}\right)$
      ▷ Solve the MPDE for the k^{th} region.
    end for
    $\mathrm{T}_h^i \leftarrow \bigcup_{k=1}^{m} \mathrm{T}_h^{(k),i}$
  end while
  $\mathrm{T}_h \leftarrow \mathrm{T}_h^i$
  $E \leftarrow Q^i$
end procedure

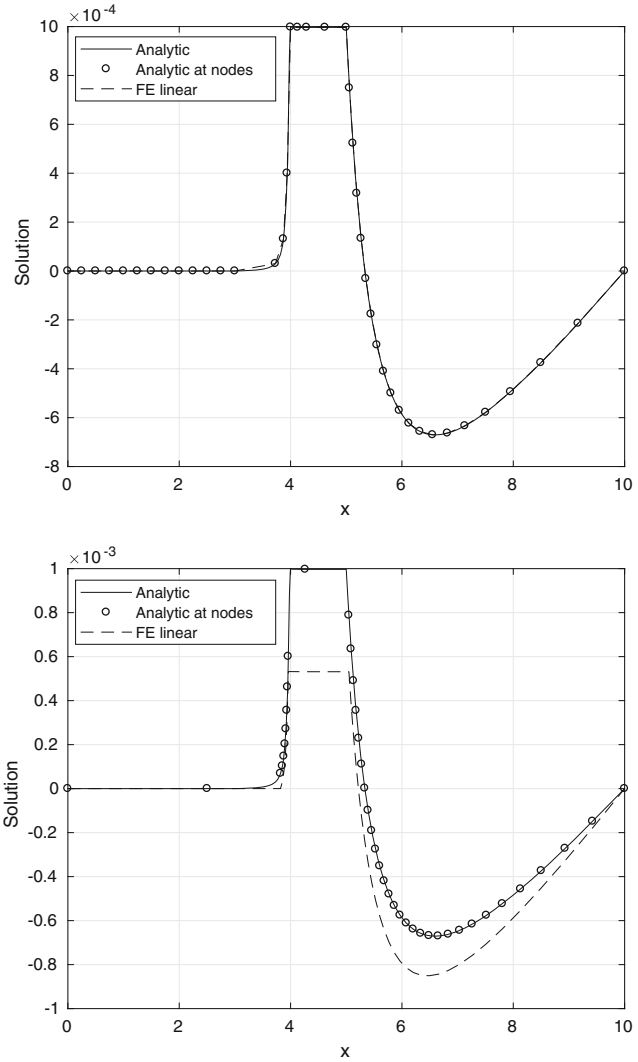

Fig. 2 Top: a solution of Eq. 54 with σ as defined in Eq. 56, and with nodes fixed at the interfaces, $x = 3$, 4, and 5. Bottom: a solution of the same problem with no fixed nodes. In both panels, the number of nodes is 41 and only r-refinement is performed

MPDE. Next, u_h, u_h^q, and z_h are updated, and a new M is evaluated; the procedure is repeated until $\|z_h\|_2$ changes by less than the prescribed tolerance.

The only differences between Algorithms 3 and 4, is that, in the latter, only the linear FE solution, u_h, is used to form the error estimate, r_h (see Section 2.1), and the procedure is continued until the level of equidistribution reaches a steady state. (The level of equidistribution, Q, is defined as $\max_{K\in\mathrm{T}_h} \theta_K - \min_{K\in\mathrm{T}_h} \theta_K$, expressed as a percentage of $\min_{K\in\mathrm{T}_h} \theta_K$.) In general, the true error of the PPDE is not available, and therefore, the only available measures to monitor the r-refinement procedure are the error estimate and the level of equidistribution. Since the ultimate goal of our hr-refinement is to reduce the solution error, the hierarchical error estimate, z_h, which accurately estimates the true error, is used as the measure for stopping the r-refinement procedure in Algorithm 3. However, the residual error estimate used here, r_h, is not an indicator of the true error, and therefore, the level of equidistribution, Q, is used to terminate Algorithm 4.

The 1D MPDE in Eq. 26 is discretized using a linear FE scheme and a fixed-point iteration method is used to solve the corresponding nonlinear BVP. The 2D linear MPDEs in Eq. 30 are also discretized using a linear FE scheme and the solutions of corresponding BVPs are followed by bilinear interpolations to derive solutions in Ω (see Section 3.7 for more details). In order to obtain smooth meshes, for both 1D and 2D cases, the Hessian-based monitor function is scaled by using the square root of $z''_{h,j}$, and the error-based monitor

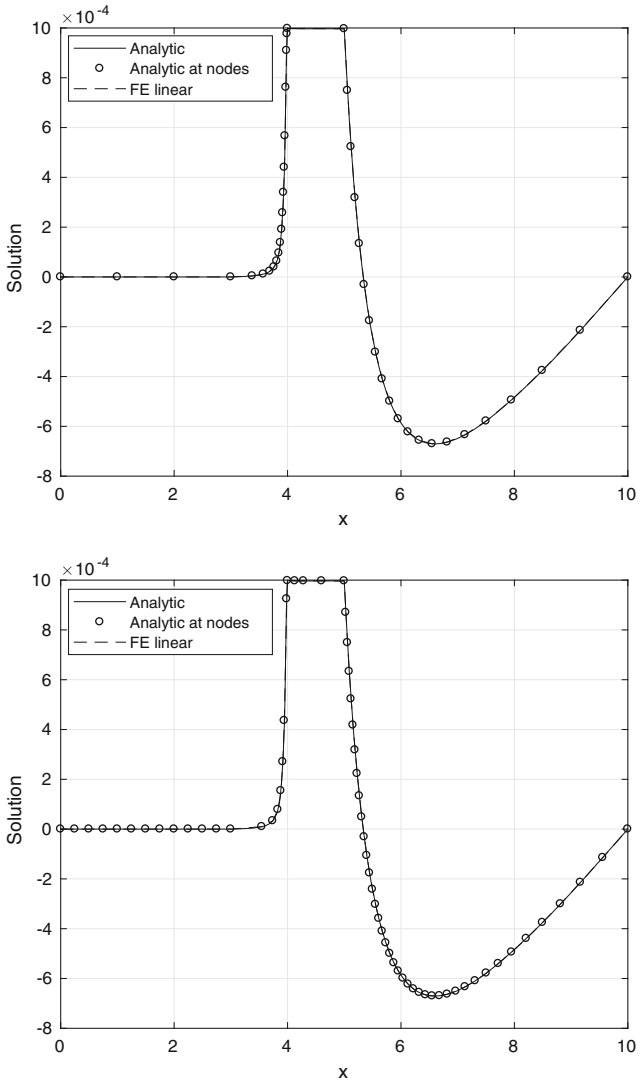

Fig. 3 Solutions of Eq. 54 with σ as defined in Eq. 56, and with nodes fixed at the interfaces, $x = 3$, 4, and 5. The starting number of nodes are 11 and 41, and the final number of nodes are 41 and 65, for the top and bottom panels, respectively

functions are scaled by using the square root of the L_2-norms of the error estimates, z_h and r_h, in Eqs. 31 and 46, respectively. In the 2D case, this scaling also helps to reduce the chance of mesh tangling. In practice, the minimum error norms that could be achieved during each *r*-refinement step were not affected by this modification. When goal-oriented error estimates are used, the error estimates z_h and r_h, in Algorithms 3 and 4, are weighted by error estimates corresponding to the solution of the adjoint problems of the main PPDE problems, as discussed in Section 2.5.

3.3 Starting grid and treatment of interfaces

In this section, we present the key findings from extensive investigations of Algorithms 1–4. Our primary study is of the 1D diffusion problem, Eq. 54, with the Helmholtz problem, Eq. 55, used for further validation. In all the figures that display 1D FE solutions, the solid lines show the true solution, evaluated at 10,000 equispaced nodes. The dashed lines show the linear FE solution, and the circles show the true solution at the grid nodes.

Figure 2 shows solutions of the diffusion problem with the four-layer model described in Section 3.1, and the hierarchical error–based monitor function. This experiment tests the effect of fixing nodes at the interfaces of the layers. Since this prevents the rest of the nodes from crossing from one region to another, *r*-refinement is, effectively, applied only within subregions. In the top panel of Fig. 2, there are fixed nodes at the interfaces of the layers (i.e., at $x = 3, 4$ and 5) while in the bottom panel there are no fixed nodes, i.e., nodes can cross the interfaces. In both examples, 41 nodes are used and no *h*-refinement is employed. While both the solutions in the top and bottom panels of Fig. 2 sufficiently equidistribute the monitor functions, it can be seen that the solution shown in the bottom panel is highly inaccurate.

In Fig. 3, the effect of the number of nodes in the initial (uniform) model is examined. In the top and bottom panels, nodes are fixed at the interfaces of the layers, the initial numbers of nodes are 11 and 41, and the final numbers of nodes are 41 and 65, respectively (i.e., one *h*-refinement and two *r*-refinements are used). Although the final numbers of nodes are different, the final error values (L_2-norm of the true errors) are roughly the same ($\approx 4.8 \times 10^{-6}$), which indicates that starting the procedure with a larger number of nodes does not necessarily result in higher accuracy.

From the two examples in this section, we conclude that it is advantageous to start the procedure with a relatively coarse mesh, and to solve the MPDE problem over each region separately. These two strategies are used for the remainder of the examples in the following sections.

3.4 Testing the monitor functions

Figure 4 gives solutions of the diffusion problem with the four-layer model, using the three monitor functions described in Section 2.4. The starting grid for all the monitor functions has 11 nodes, and the *hr*-refinement is continued until the equidistribution of the monitor functions is reached. Four, three, and three *hr*-refinement iterations (of the main procedure, Algorithm 1) are used for the solutions using the hierarchical error–based, hierarchical Hessian–based and residual error–based monitor functions, respectively (resulting in five, four, and four grids for each solution, respectively). For each monitor function, final solutions (i.e., after *r*-refinement) for four grids are shown in the figure, and the corresponding true error L_2-norms are given in Fig. 5. These two figures show that the three

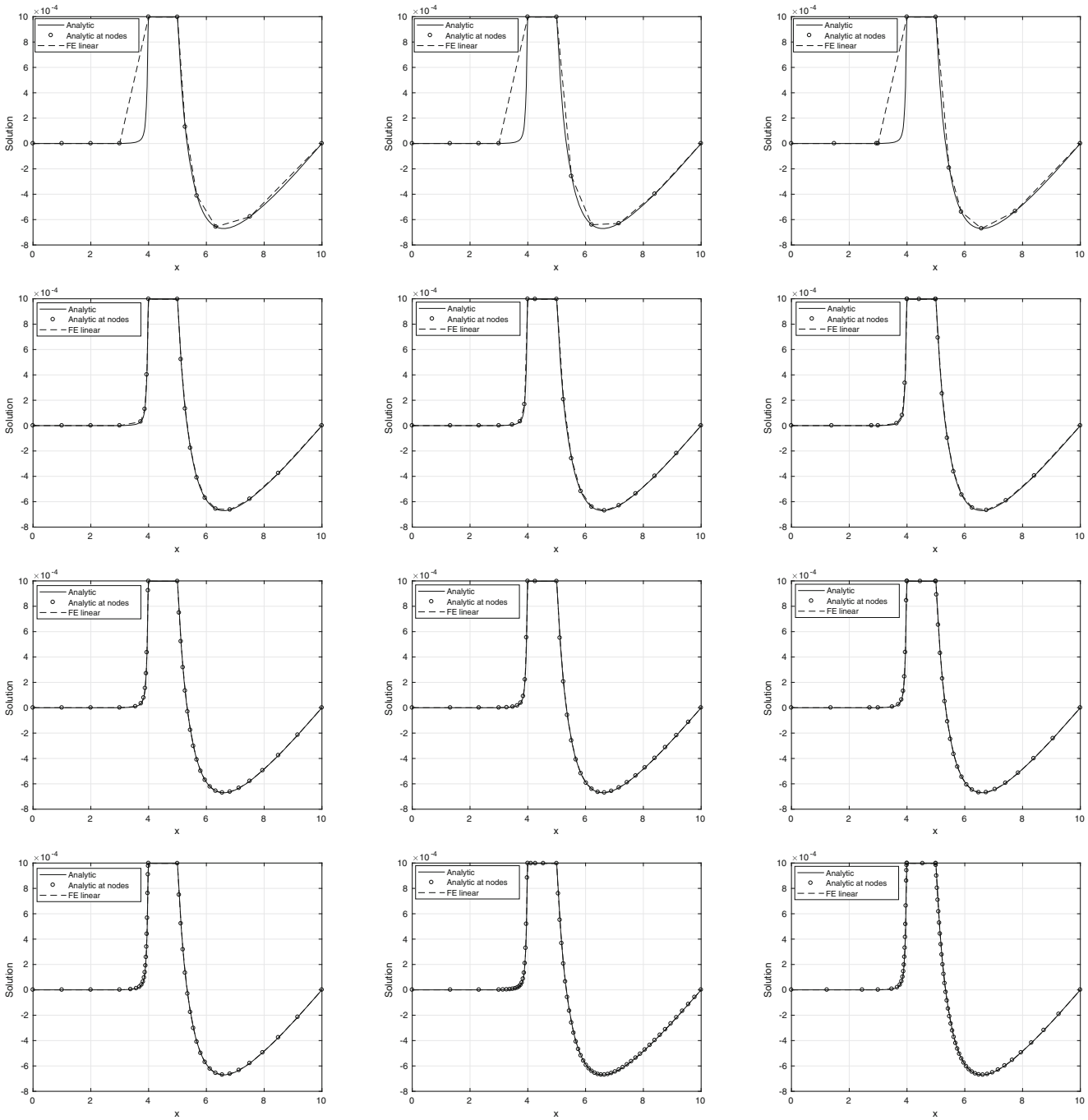

Fig. 4 Solutions of Eq. 54 with σ as defined in Eq. 56, and with nodes fixed at the interfaces, using different monitor functions. The left, middle, and right panels use the hierarchical error–based, hierarchical Hessian–based, and residual error–based monitor functions, respectively. The four rows of panels correspond to three h-refinements. All the panels show solutions after r-refinement. The L_2-norms of the true error corresponding to each of these panels are given in Fig. 5

monitor functions are very similar in terms of the final solutions obtained, the final error values that are reached, and the rate of convergence of error. Since the hierarchical error–based monitor function is based on error, it is more natural than the Hessian-based monitor function. Also, as will be shown in the next section, the hierarchical error estimate has an important advantage over the residual error estimate in that it approximates the true error more closely. Therefore, due to the similarity observed between the monitor functions in Figs. 4 and 5, we use the hierarchical error–based monitor function for all subsequent numerical experiments.

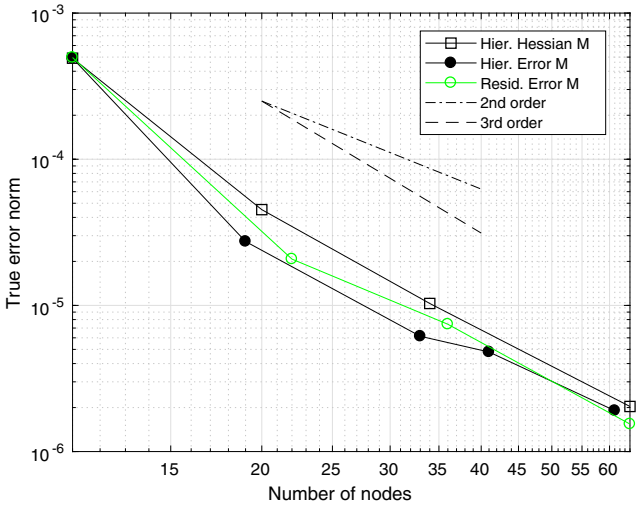

Fig. 5 L_2-norms of true error versus the number of nodes for the results in Fig. 4. The solid circles, squares, and empty circles correspond to the hierarchical error–based, hierarchical Hessian–based and residual error–based monitor functions, respectively. The dashed and dash-dotted lines show cubic and quadratic convergence rates, respectively

3.5 Stopping criteria

As explained in Section 3.2, there are three possible measures to control the *r*-refinement: the true error, which is in general unavailable; the error estimate; and the level of equidistribution of the monitor function (defined as Q in Section 3.2). The last two measures are used for the termination criteria in Algorithms 3 and 4, respectively. Figure 6 summarizes the results of extensive numerical experiments on these measures for the solution of the diffusion problem using the hierarchical error-based monitor function. The four distinct curves in each panel correspond to four grids with 21, 37, 65, and 81 nodes (so, three *h*-refinements), and the hierarchical error estimate is used to stop the *r*-refinement for each of the four grids. Despite occasional mismatches, it can be seen that the hierarchical error estimate approximates the true error very well, and therefore, it can be relied on as a measure to monitor the *r*-refinement procedure. The level of equidistribution, Q, is also a viable measure. However, the trend in Q does not always follow the trend in the error. Therefore, only if the error estimate is not a good indicator of the true error, such as r_h used in this study, should we use Q as the measure to control the *r*-refinement.

An additional observation from Fig. 6 is that the finest grids require fewer *r*-refinement steps (of Algorithm 3) to reach convergence (here, reaching a steady-state in terms of the error estimate). The grids with 21, 37, 65, and 81 nodes require four, four, three, and two *r*-refinement iterations, respectively. This means that starting the *hr*-refinement procedure with the *r*-refinement of a relatively coarse mesh

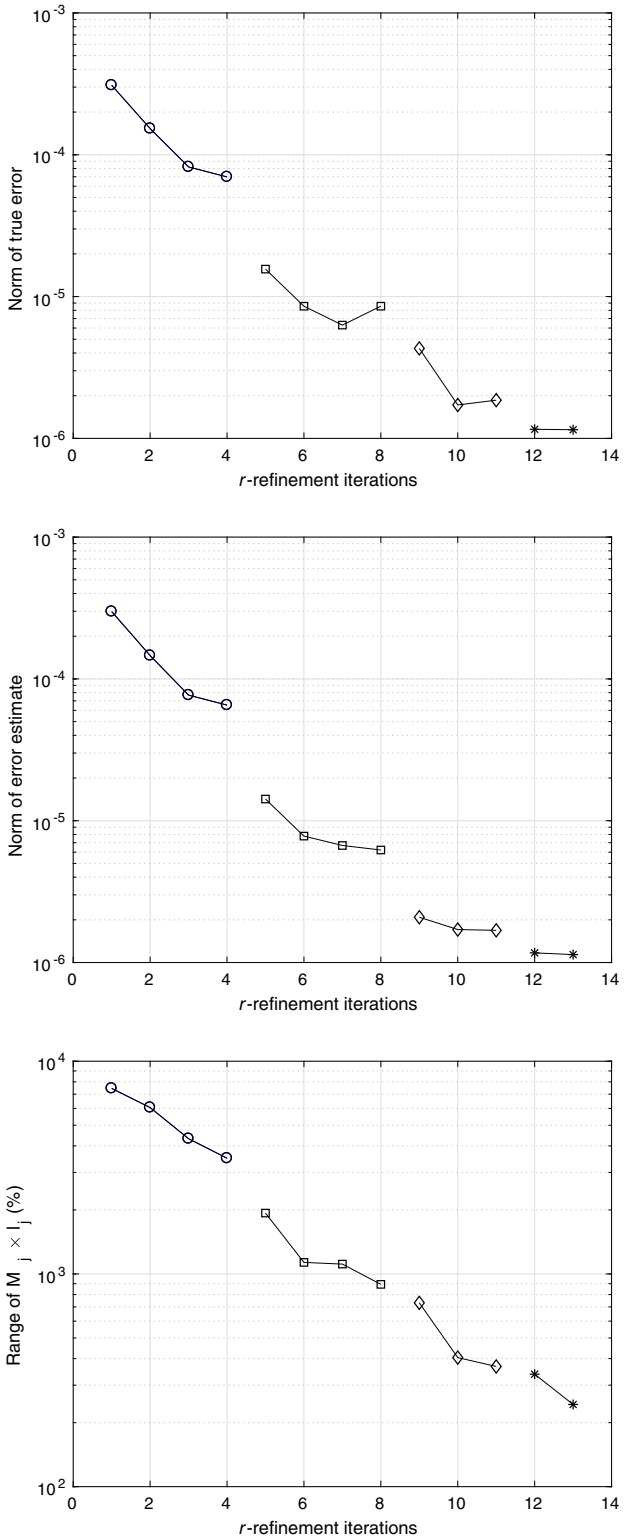

Fig. 6 The L_2-norm of true error and hierarchical error estimate (top and middle, respectively) and the level of equidistribution (defined as Q in Section 3.2) (bottom panel) versus the number of *r*-refinement steps. (The entire procedure used 13 *r*-refinement steps of Algorithm 3.) The circles, squares, diamonds, and asterisks correspond to grids with 21, 37, 65, and 81 nodes, respectively. The problem in Eq. 54 with σ as defined in Eq. 56, is used

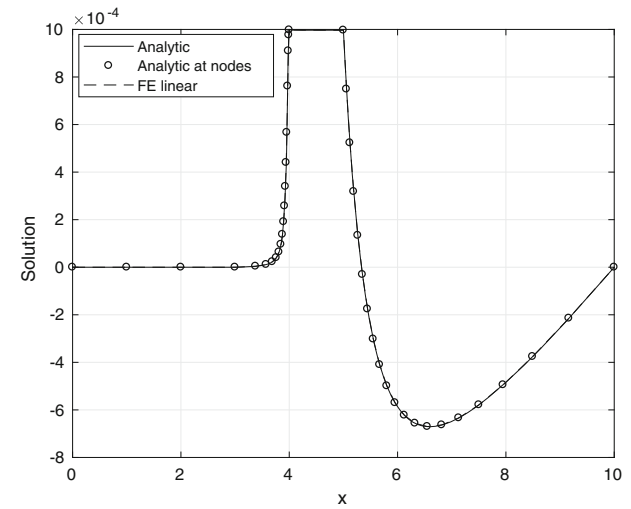

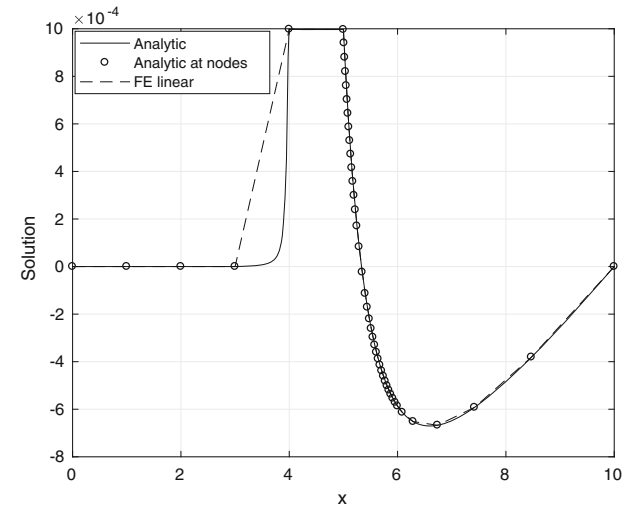

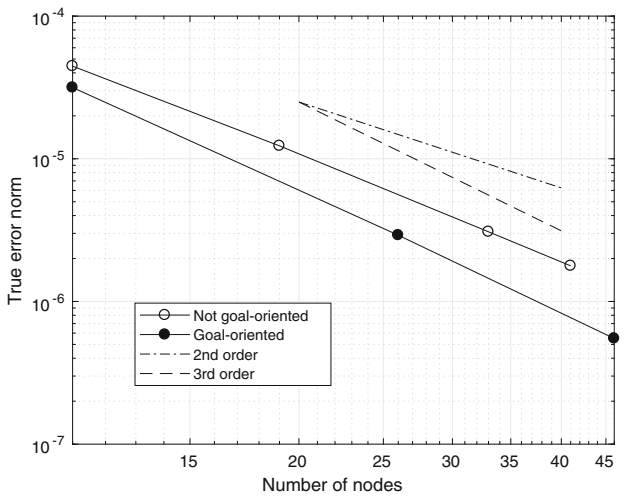

Fig. 7 Solutions of Eq. 54 with σ as defined in Eq. 56, with the global and goal-oriented *hr*-refinement techniques (top and middle panels, respectively), and their corresponding convergence curves (bottom). The solutions in the top and middle panels correspond to the final grids with 41 and 46 nodes, respectively. The L_2-norms measure the error inside the target region, $x \in [5, 6]$, only

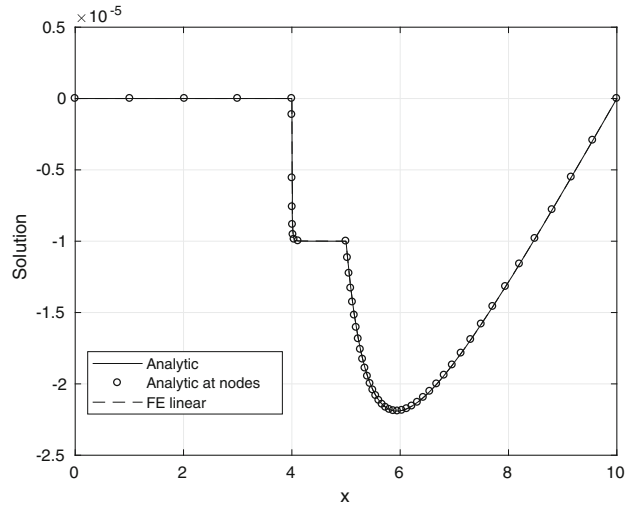

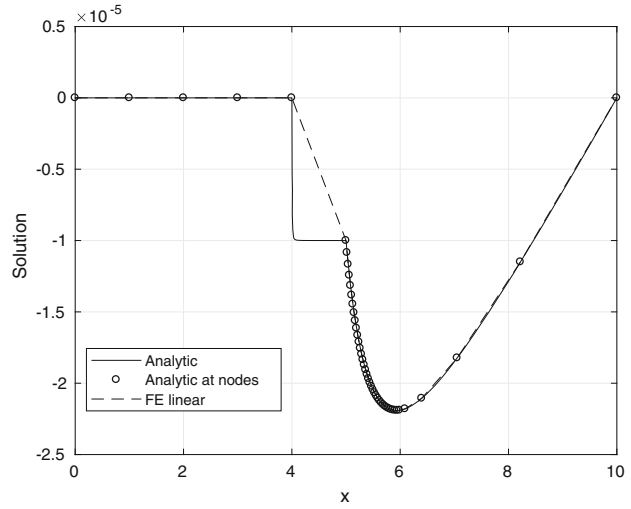

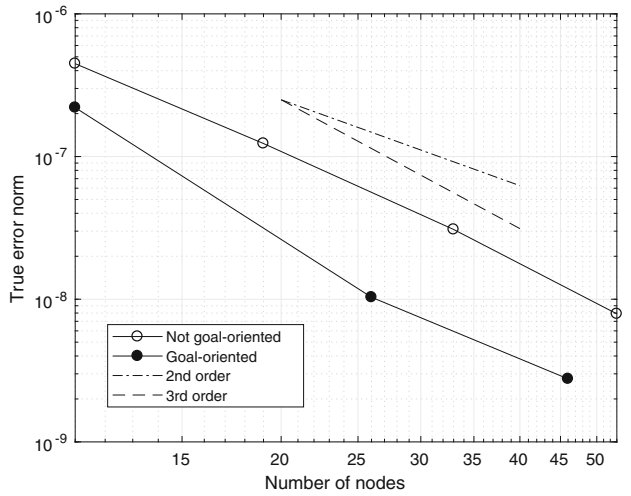

Fig. 8 Solutions of Eq. 54 with σ as defined in Eq. 57, and $c = 200$ in Eq. 59. The top and middle panels show solutions with the global and goal-oriented *hr*-refinement techniques, respectively, and their corresponding convergence curves are given at the bottom panel. The solutions in the top and middle panels correspond to the final grids with 53 and 46 nodes, respectively. The L_2-norms measure the error inside the target region, $x \in [5, 6]$, only

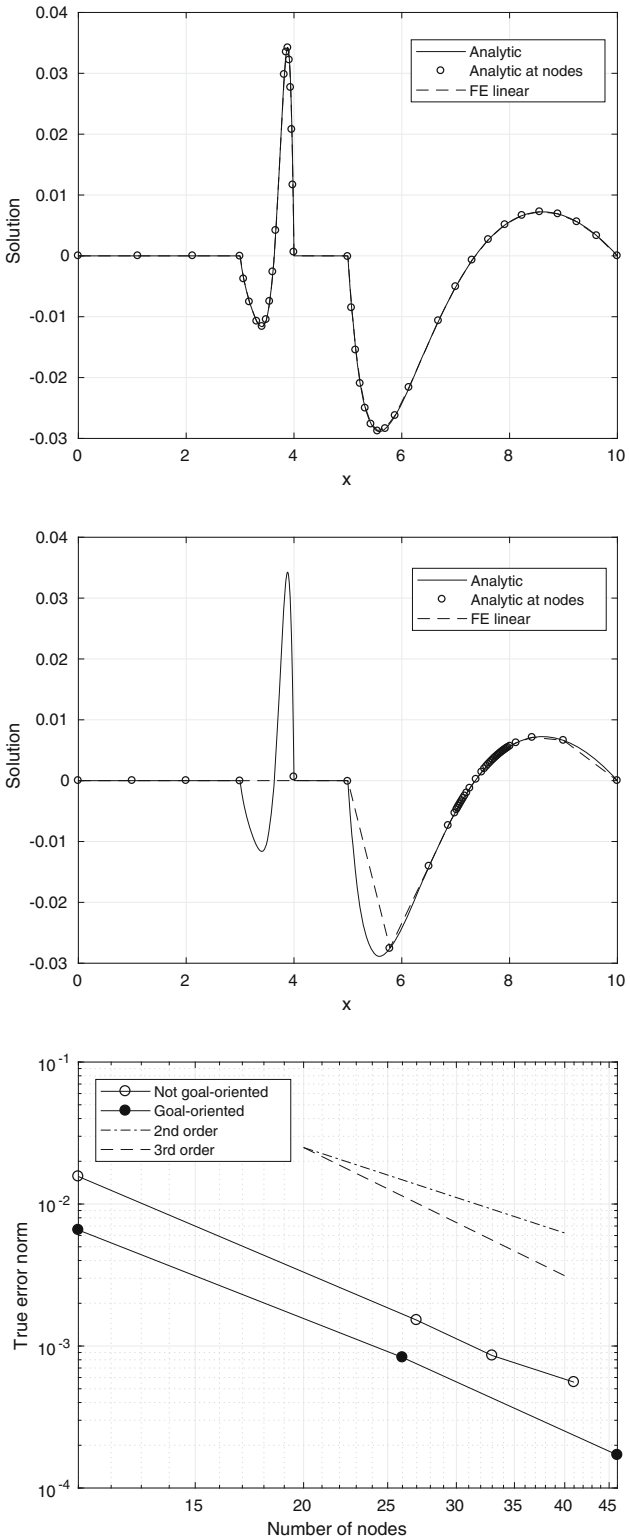

Fig. 9 Solutions of Eq. 55, with σ as defined in Eq. 58. In the source term, Eq. 59, $c = 2$ is used. The top and middle panels show solutions with the global and goal-oriented *hr*-refinement techniques, respectively, and their corresponding convergence curves are given at the bottom panel. The solutions in the top and middle correspond to the final grids with 41 and 46 nodes, respectively. The L_2-norms measure the error inside the target region, $x \in [7, 8]$, only

(e.g., here with 21 nodes) can help to avoid more expensive *r*-refinement of finer grids (e.g., here the last grid with 81 nodes). It should also be noted that the numbers of *r*-refinement steps observed here are typical, i.e., the initial grids usually require 3–4 steps to converge, but after 2 or 3 *h*-refinements this is typically reduced to about 2 steps.

3.6 Examples with goal-oriented refinement

With a goal-oriented *hr*-refinement, we hope to achieve a particular error norm in a specific part of the domain more efficiently than using a global *hr*-refinement of the same grid. Figures 7, 8, and 9 present solutions of the diffusion and Helmholtz problems, Eqs. 54 and 55, respectively, and the corresponding error norms at target regions, using both goal-oriented and global refinements of the models with the hierarchical error–based monitor function. Target regions in geophysical applications can be defined as a set of discrete observation points or, alternatively, continuous regions which contain observation locations. Therefore, the size and shape of these regions can be varied, depending on the number and distribution of observation locations. For the one-dimensional case, we choose an arbitrary segment as the region of interest. This segment can be seen as a region which contains a vertical profile of observation points. These segments are chosen in the air region where the solutions show relatively higher gradients.

Figure 7 shows solutions of the diffusion problem with global (top) and goal-oriented (middle) refinements where the target region for the goal-oriented refinement is at $x \in [5, 6]$. The solution with global refinement shows a balanced distribution of the nodes over the entire domain while the solution obtained with goal-oriented refinement concentrates most of the nodes inside the target region. This figure also shows the convergence of true error norm inside the target region for both solutions. The rates of convergence are roughly similar. However, it is clear that lower error values can be achieved by the goal-oriented refinement, with the same number of grid nodes. To verify this conclusion, another example with a different σ and source term is presented in Fig. 8. In this example, the diffusion problem is used with the same four-layer model but with σ as defined in Eq. 57. Also, in this example, the Gaussian-like source is narrower, with $c = 200$ in Eq. 59. It can be seen that, again, the solution obtained with the goal-oriented refinement concentrates most of the nodes in the target region, and the error values for this solution are lower than those for the solution computed with global refinement of the grid.

The comparison conducted above is repeated for the Helmholtz problem, Eq. 55, in Fig. 9. This example uses the same four-layer model but with σ as defined in Eq. 58. Also, in the source term, Eq. 60, $c = 2$ is used. As mentioned

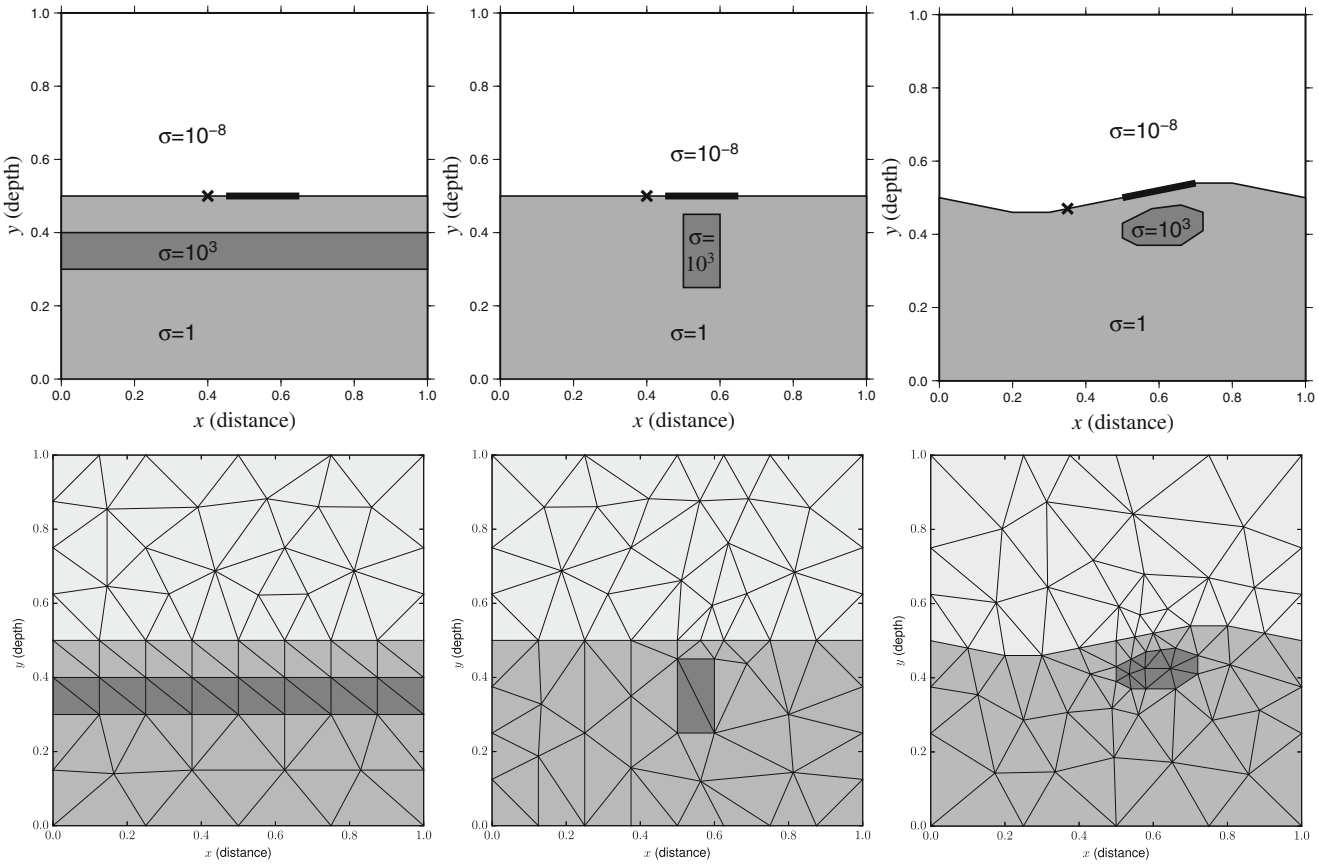

Fig. 10 Top, left to right: the layered and block-in-halfspace models and the realistic model used for the 2D examples. The σ values are used in Eq. 63. The cross symbol and the thick line segment show the locations of the singular source and the observation points, respectively. The domain is composed of air and ground regions and anomalous regions located inside the ground. Bottom: the starting coarse grids used for these three models

earlier, σ and c values are chosen such that the solutions are challenging enough to necessitate refinement. The target region for the goal-oriented refinement is chosen to be at $x \in [7, 8]$. It can be seen that, for these solutions, too, the results with goal-oriented refinement are more accurate, with the same level of refinement, compared to the results using global refinement. Also, the final solution on the finest goal-oriented grid shows that most of the nodes are concentrated in the target region while the solution with global refinement shows a balanced distribution of the nodes over the domain.

3.7 Examples in 2D

The *hr*-refinement algorithm proposed and verified in the previous sections is further validated here using 2D examples. The linear MPDEs given by Eq. 30 are used here for *r*-refinements, and both uniform and local *h*-refinements are applied. Here, the open-source software FEniCS [2, 39] is used for the initial triangular mesh generation and for the FE solution of the PPDE and MPDE problems. All of the resulting discretized systems (both MPDEs and PPDEs) are solved using algebraic multigrid-preconditioned CG. For brevity and since the Helmholtz problem is more challenging than the diffusion problem, only Eqs. 10 and 11 are considered for the 2D case. For Eq. 10, the test problem used here is given by

$$\begin{cases} -\nabla^2 u + \sigma(\boldsymbol{x})\, u = f(\boldsymbol{x}), \quad \boldsymbol{x} \in \left(x^l, x^r\right) \times \left(y^b, y^t\right) \\ u(\boldsymbol{x})\Big|_{\substack{x=x^l \\ x=x^r}} = 0, \quad u(\boldsymbol{x})\Big|_{\substack{y=y^b \\ y=y^t}} = 0, \end{cases} \tag{63}$$

where $x^l = y^b = 0$ and $x^r = y^t = 1$. The physical domain, $\Omega = \left[x^l, x^r\right] \times \left[y^b, y^t\right]$, represents three models. The first model is a layered halfspace which is the 2D equivalent of the model used for the 1D examples. In this model, the interfaces of the layers are at $y = 0.3$, 0.4, and 0.5, and for these four layers from $y = 0$ to 1, the coefficient values are $\sigma = 1$, 10^3, 1, and 10^{-8}, respectively (see Fig. 10). The second model is a block-in-halfspace comprising air and ground regions at $y > 0.5$ and $y < 0.5$, and with $\sigma = 10^{-8}$ and $\sigma = 1$, respectively, and an anomalous rectangular region located inside the ground at $[0.5, 0.6] \times [0.25, 0.45]$,

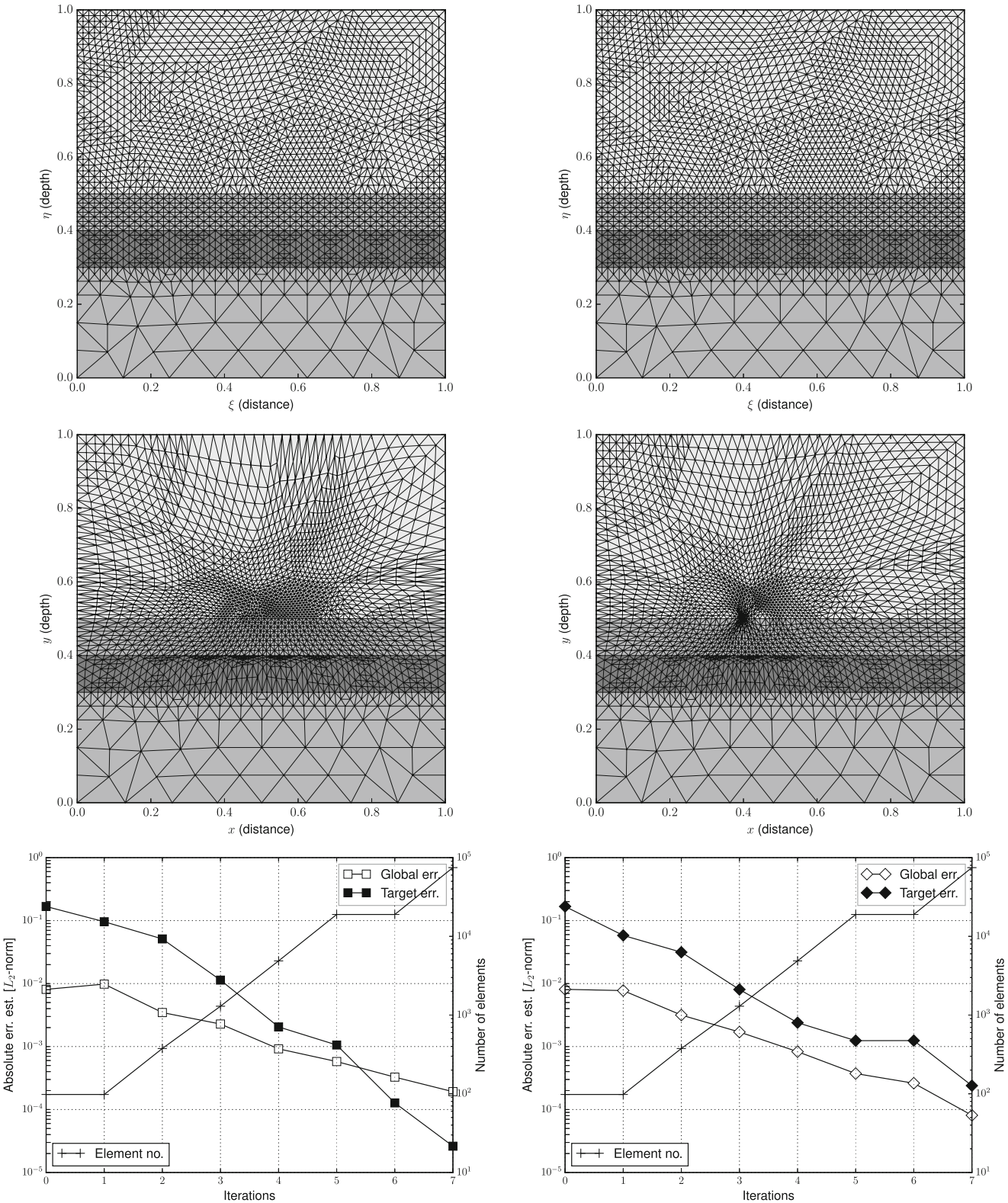

Fig. 11 A goal-oriented *hr*-adaptivity for the solution of Eq. 63, with the layered halfspace model in Fig. 10. Top and middle panels: the computational and physical meshes at the end of the 5th iteration, respectively. Bottom: the norm of error estimate at the target and over the entire mesh, and the number of elements for the *h*- and *r*-refinement iterations

Fig. 12 A global *hr*-adaptivity for the solution of Eq. 63, with the layered halfspace model in Fig. 10. Top and middle panels: the computational and physical meshes at the end of the 5th iteration, respectively. Bottom: the norm of error estimate at the target and over the entire mesh, and the number of elements for the *h*- and *r*-refinement iterations

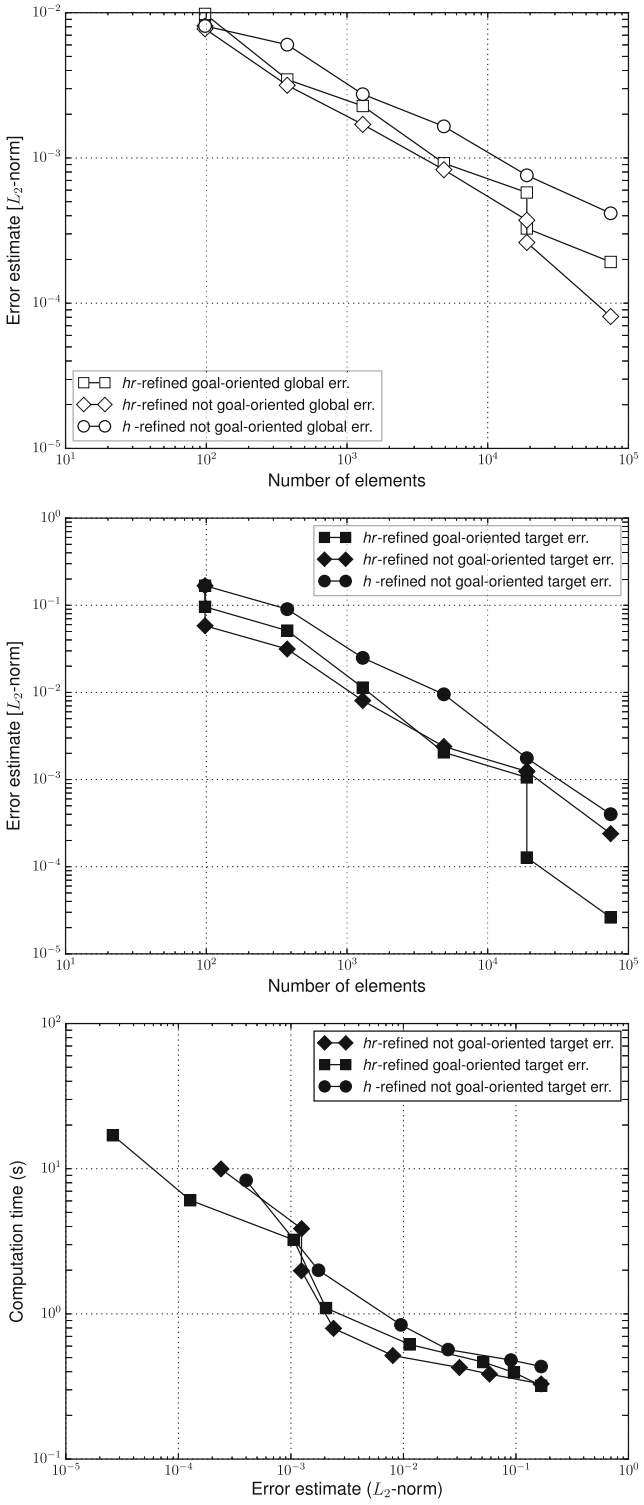

Fig. 13 The L_2-norm of error estimate over the entire mesh (top) and at the target (middle) versus the number of elements for global and goal-oriented solutions of Eq. 63, with the layered halfspace model in Fig. 10. Bottom: the L_2-norm of error estimate at the target versus computation time. Results with both (pure) *h*-refinement and with *hr*-refinement are depicted. The results with *hr*-refinement correspond to the error values in the bottom panels of Figs. 11 and 12

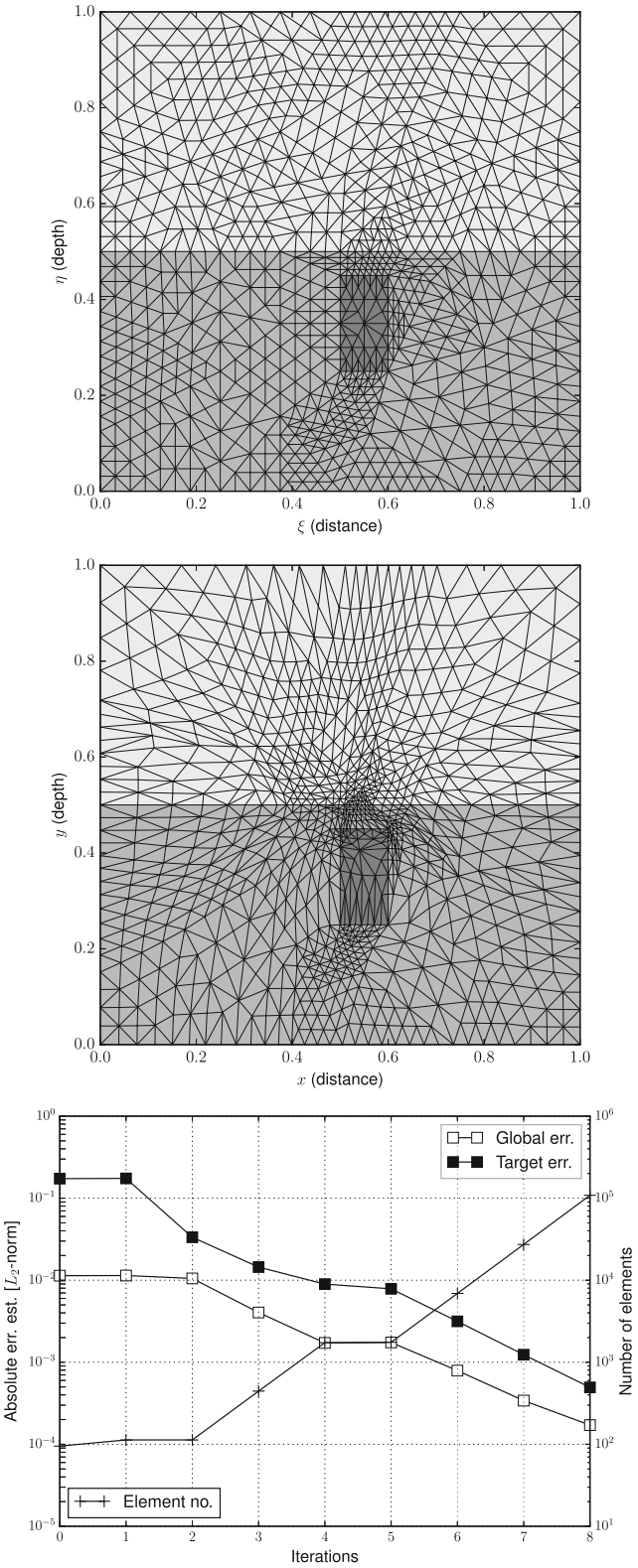

Fig. 14 A goal-oriented *hr*-adaptivity for the solution of Eq. 63, with the block-in-halfspace model in Fig. 10. Top and middle panels: the computational and physical meshes at the end of the 5th iteration, respectively. Bottom: the norm of error estimate at the target and over the entire mesh, and the number of elements for the *h*- and *r*-refinement iterations

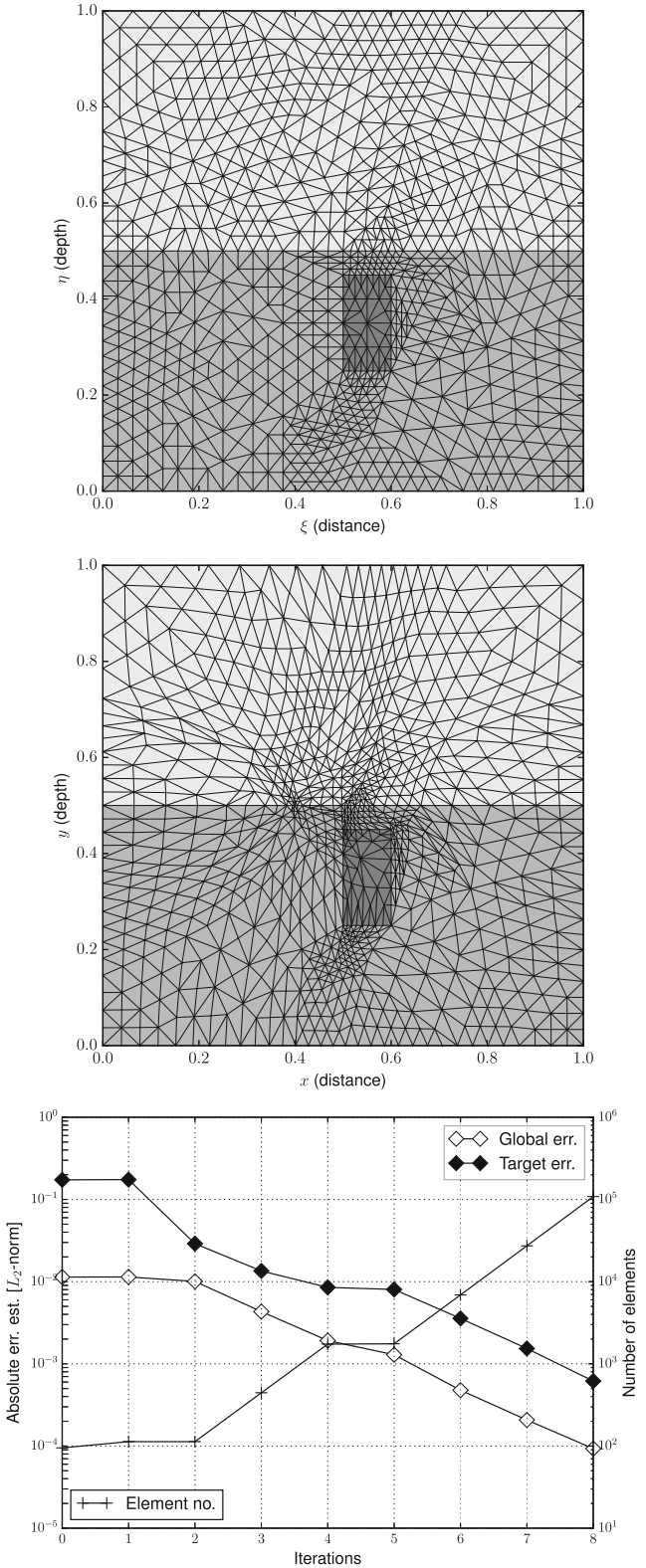

Fig. 15 A global *hr*-adaptivity for the solution of Eq. 63, with the block-in-halfspace model in Fig. 10. Top and middle panels: the computational and physical meshes at the end of the 5th iteration, respectively. Bottom: the norm of error estimate at the target and over the entire mesh, and the number of elements for the *h*- and *r*-refinement iterations

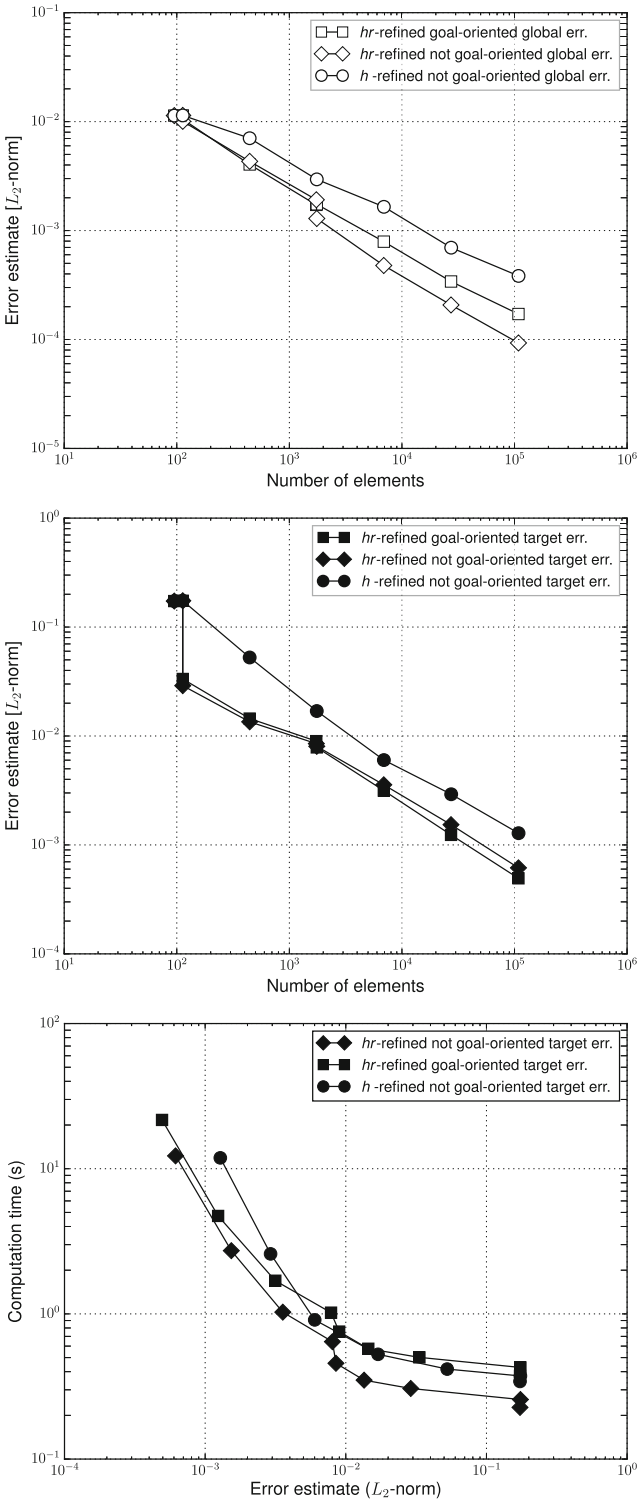

Fig. 16 The L_2-norm of error estimate over the entire mesh (top) and at the target (middle) versus the number of elements for global and goal-oriented solutions of Eq. 63, with the block-in-halfspace model in Fig. 10. Bottom: the L_2-norm of error estimate at the target versus computation time. Results with both (pure) *h*-refinement and with *hr*-refinement are depicted. The results with *hr*-refinement correspond to the error values in the bottom panels of Figs. 14 and 15

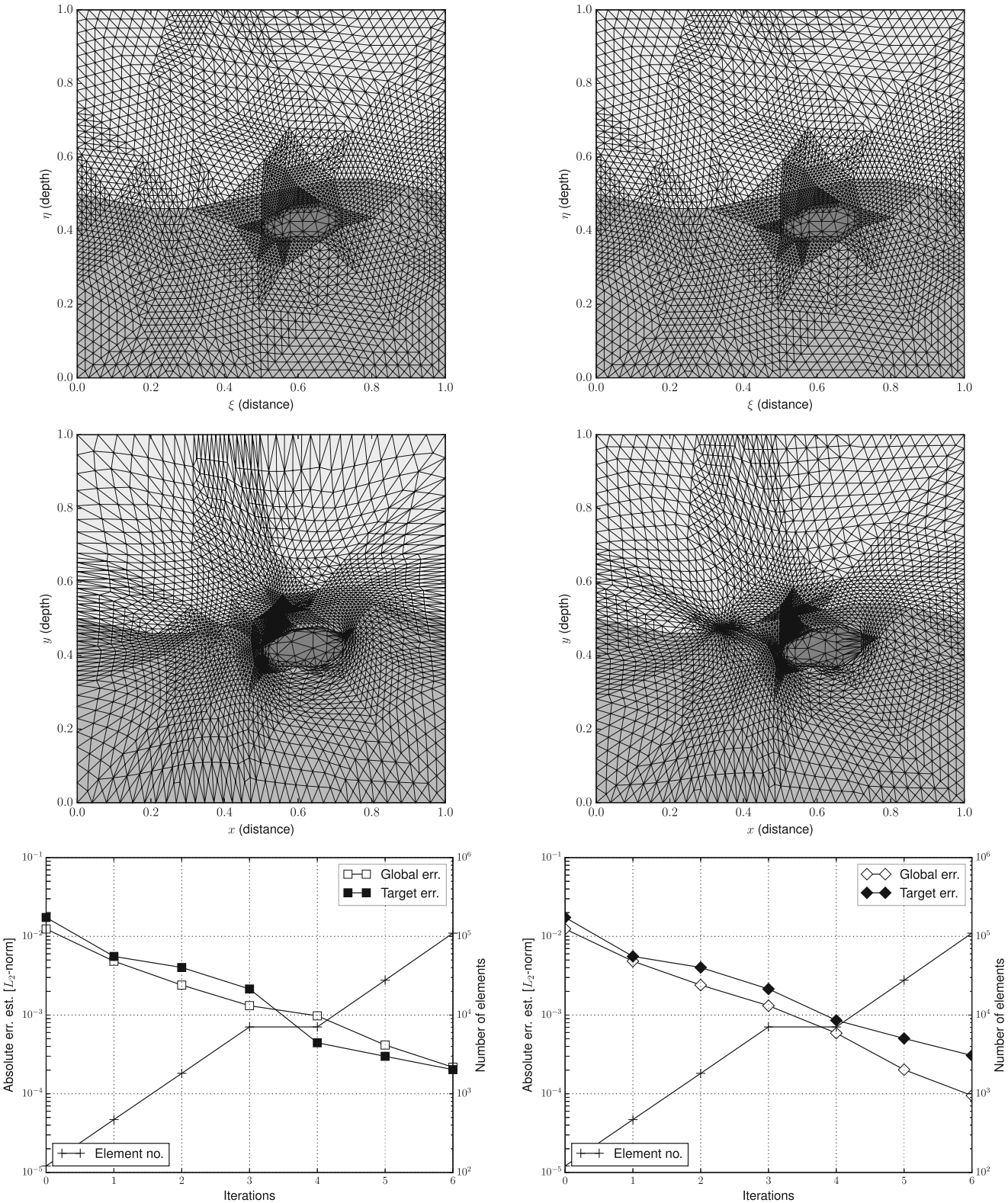

Fig. 17 A goal-oriented *hr*-adaptivity for the solution of Eq. 63, with the realistic model in Fig. 10. Top and middle panels: the computational and physical meshes at the end of the 4th iteration, respectively. Bottom: the norm of error estimate at the target and over the entire mesh, and the number of elements for the *h*- and *r*-refinement iterations

Fig. 18 A global *hr*-adaptivity for the solution of Eq. 63, with the realistic model in Fig. 10. Top and middle panels: the computational and physical meshes at the end of the 4th iteration, respectively. Bottom: the norm of error estimate at the target and over the entire mesh, and the number of elements for the *h*- and *r*-refinement iterations

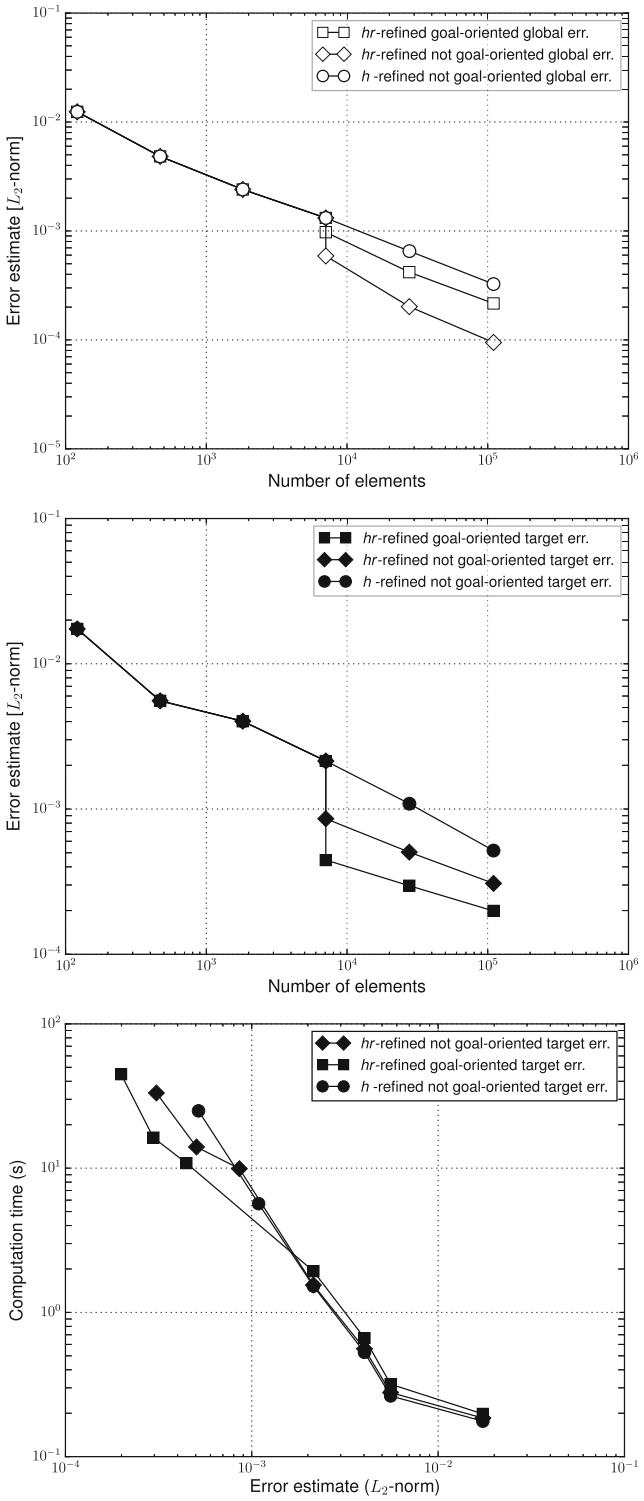

Fig. 19 The L_2-norm of error estimate over the entire mesh (top) and at the target (middle) versus the number of elements for global and goal-oriented solutions of Eq. 63, with the realistic model in Fig. 10. Bottom: the L_2-norm of error estimate at the target versus computation time. Results with both (pure) *h*-refinement and with *hr*-refinement are depicted. The results with *hr*-refinement correspond to the error values in the bottom panels of Figs. 17 and 18

with $\sigma = 10^3$. The target in these models consists of 21 equidistant observation points along a horizontal profile at $x = 0.45$–0.65, $y = 0.5$ (see Fig. 10). As for the 1D case, σ values are chosen to represent common underground conductivity contrasts. If (x_s, y_s) gives the source location, for the two models described above, $(x_s, y_s) = (0.4, 0.5)$. The third model is more realistic in the sense that the air-ground interface is uneven and the anomalous region is no longer a rectangle (see Fig. 10). The σ values in the third model are the same as in the second model and $(x_s, y_s) = (0.35, 0.47)$. The target consists of 21 equidistant observation points along a linear profile at the air-ground interface with coordinates ranging from $x = 0.5$-0.7, $y = 0.5$–0.54 (see Fig. 10).

For the PPDE in Eq. 11, the test problem is given by

$$\begin{cases} \nabla \cdot \mu_0^{-1} \nabla u - i\omega\sigma(\boldsymbol{x})\, u = f(\boldsymbol{x}), & \boldsymbol{x} \in \left(x^l, x^r\right) \times \left(y^b, y^t\right) \\ u(\boldsymbol{x})\big|_{\substack{x=x^l \\ x=x^r}} = 0, \quad u(\boldsymbol{x})\big|_{\substack{y=y^b \\ y=y^t}} = 0, \end{cases} \tag{64}$$

where $x^l = y^b = -1000$ m and $x^r = y^t = 1000$ m. The physical domain, $\Omega = \left[x^l, x^r\right] \times \left[y^b, y^t\right]$, represents a block-in-halfspace. The σ (conductivity) values of the ground and the block are $1/30$ and $100/3$ S/m, respectively, and the block occupies the region given by $[-3.35, 3.35] \times [-52, -10]$ m. We choose 36 equidistant observation points along a profile at $x = [-80, 100]$ m, $z = 0$ m. In this model, the source is located at $(x_s, z_s) = (-139.6, 0)$ m and operates at $\tilde{f} = 400$ Hz.

It was concluded in Section 3.3 that it is advantageous to preserve the interfaces between the regions by fixing nodes at these locations. The 2D equivalent of that is to maintain nodes at the internal (and external) boundaries but allow them to move along these interfaces, during *r*-refinement, for higher accuracy. For the 2D models, with vertical or horizontal internal and external boundaries, the MPDEs can be solved as BVPs with mixed boundary conditions, given by

$$\begin{cases} \nabla \cdot \left(M^{-1} \nabla \xi\right) = 0, & \boldsymbol{x} \in \left(x^l, x^r\right) \times \left(y^b, y^t\right), \\ \xi(\boldsymbol{x}) = x, & \forall\, \boldsymbol{x} \in \partial\Omega_c\big|_{\hat{\boldsymbol{n}}=\hat{\boldsymbol{e}}_x}, \\ \nabla\xi(\boldsymbol{x}) \cdot \hat{\boldsymbol{n}} = 0, & \forall\, \boldsymbol{x} \in \partial\Omega_c\big|_{\hat{\boldsymbol{n}}=\hat{\boldsymbol{e}}_y}, \end{cases} \tag{65}$$

and

$$\begin{cases} \nabla \cdot \left(M^{-1} \nabla \eta\right) = 0, & \boldsymbol{x} \in \left(x^l, x^r\right) \times \left(y^b, y^t\right), \\ \eta(\boldsymbol{x}) = y, & \forall\, \boldsymbol{x} \in \partial\Omega_c\big|_{\hat{\boldsymbol{n}}=\hat{\boldsymbol{e}}_y}, \\ \nabla\eta(\boldsymbol{x}) \cdot \hat{\boldsymbol{n}} = 0, & \forall\, \boldsymbol{x} \in \partial\Omega_c\big|_{\hat{\boldsymbol{n}}=\hat{\boldsymbol{e}}_x}, \end{cases} \tag{66}$$

where $\partial\Omega_c$ represents any internal or external boundary of Ω_c, $\hat{\boldsymbol{n}}$ denotes the unit normal to $\partial\Omega_c$, and $\hat{\boldsymbol{e}}_x$ and $\hat{\boldsymbol{e}}_y$ are unit vectors parallel to the *x*- and *y*-axes, respectively. M in Eqs. 65 and 66 is a scalar monitor function corresponding to the current physical mesh, T_h. The MPDE problems are discretized and solved on T_h and their solutions constitute

the coordinates of the nodes of a mesh designated here as T_c^*. Since T_c^* is in Ω_c while the PPDEs are solved in Ω here, T_c^* should be mapped to Ω using $\boldsymbol{x} = (x(\xi, \eta), y(\xi, \eta))$.

When the internal boundaries of the model are not vertical or horizontal, as is the case with the realistic model in the right panels of Fig. 10, we apply an additional stage in which we first map the mesh with irregular interfaces, T_h, to a new mesh, T_h^*, where all the interfaces are either vertical or horizontal. This mapping is performed by solving a pair of Laplace equations on T_h with appropriate boundary conditions (see, e.g., [22]). We then solve the BVPs in Eqs. 65 and 66 on T_h^* and obtain T_c^* which is in Ω_c. Afterwards, T_c^* is mapped to Ω, using bilinear interpolation, which results in T_h^{**}. (We note that all the interfaces in T_h^*, T_c^* and T_h^{**} are either vertical or horizontal). Finally, T_h^{**} is mapped back into a new mesh, in Ω, with the original irregular interfaces, by solving a second pair of Laplace equations, with appropriate boundary conditions.

Following Algorithms 1–3 and the conclusions of the previous sections, the procedure starts with a relatively coarse mesh (Fig. 10, bottom panels) which is then *hr*-refined until a desired error norm is reached. Here, the hierarchical error–based monitor function, Eq. 35, is used and the hierarchical error estimate is used as the stopping criterion. The coordinate transformation is approximated by an affine mapping between the nodes of T_h and T_c^* and the new physical mesh is found by interpolation at the nodes of T_c. Following Algorithm 3, M is then updated using the new T_h, the MPDEs are solved to derive a new T_c^* and the interpolation step is repeated. Note that unlike T_c^*, which is updated at each iteration of Algorithm 3, T_c is fixed throughout this algorithm. Following Algorithms 1 and 2, the monitor function from the final solution of the *r*-refinement is used as a measure to calculate the number of *h*-refinements needed for each of the subdomains.

Figures 11, 12, 13, 14, 15, 16, 17, 18, and 19 show examples of global and goal-oriented *hr*-adaptivity for the solution of the Helmholtz problem, Eq. 63, with the three corresponding 2D models described above. In Figs. 11, 12, 14, 15, 17, and 18, example T_c and T_h grids are given at the top and middle panels, respectively. (The final grids are too dense to show here.) The panels at the bottom of these figures give the L_2-norm of error estimate at the target and over the entire grid, and the number of elements for the *h*- and *r*-refinement iterations. Note that, in these panels, if the number of elements stays constant this indicates an *r*-refinement iteration (of Algorithm 3) and an increase in this number means an *h*-refinement (Algorithm 2). Also note that, here, as for the 1D case, the initial coarse mesh and each of the subsequent *h*-refined meshes are *r*-refined. However, only solutions which reduce the error estimate are preserved, which explains the consecutive *h*-refinements without intermediate *r*-refinements, observed in the bottom panels of the figures mentioned above.

Figures 11–13 show solutions of the Helmholtz problem with the layered halfspace model, Figs. 14–16 with the block-in-halfspace model and Figs. 17–19 with the realistic model (irregular interfaces). Figures 11, 14, and 17 use goal-oriented error estimates and Figs. 12, 15, and 18 use global error estimates. Figures 13, 16, and 19 compare the error norms of the solutions at the target and over the entire grid with global and goal-oriented *hr*-refinements and with pure *h*-refinements. These figures also give the computation time to reach the given error norms with pure *h*-refinement and with global and goal-oriented *hr*-refinements. It can be seen that, as for the 1D case, higher accuracies at the targets are achieved using the goal-oriented error estimates. It can also be seen that the *hr*-refinements are more efficient than the pure *h*-refinements, in terms of computation time. Moreover, we see that, despite the additional time required to solve the adjoint problems, the goal-oriented *hr*-refinements are, in general, more efficient than the global *hr*-refinements.

Additionally, a comparison between the middle panels in Figs. 13, 16, and 19 reveals that goal-oriented *hr*-adaptivity is relatively less effective in the second and third examples, compared to the first example (layered halfspace). In the second and third examples, the closeness of the anomalous regions to the observation profiles pushes *h*-refinement and global *r*-refinement to give higher refinements at the observation profiles (see the top and middle panels in Figs. 15 and 18), which reduces the relative effectiveness of the goal-oriented *hr*-refinements in these two examples. However, in the layered halfspace example, *h*-refinement and global *r*-refinement do not give high refinement at the observation profile (see the top and middle panels in Fig. 12), and the goal-oriented *hr*-refinement is relatively more effective in reducing the target error norm.

Figures 20, 21, and 22 show an example of goal-oriented *hr*-adaptivity for the solution of the TE mode problem in Eq. 64, where the source represents an infinitely long wire at the air-ground interface and extended along the conductivity strike, i.e., the z-axis. Since, in this example, the dimensions of Ω, relative to the size of the anomalous region, are much larger than those in the previous 2D examples, we use local *h*-refinements here for higher efficiency. We use the *r*-refinement monitor function as the parameter to mark the elements to be refined, and we consider two different *h*-refinement methods. In the pure *h*-refinement case, we use the popular "maximum" strategy, based on refining a fixed fraction (here 15%) of the elements with the highest values of the monitor function. For *hr*-refinement, we employ an alternative "equilibration" method, based on marking the elements over which the sum of the monitor function values

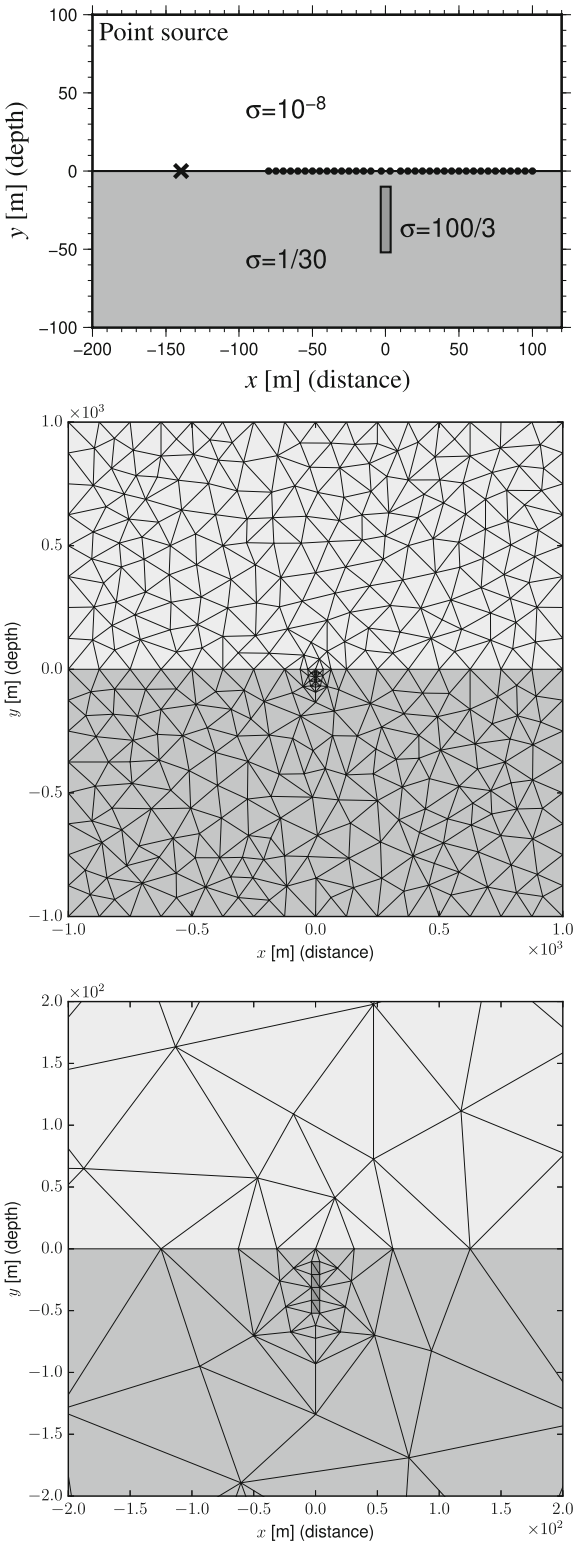

Fig. 20 Top: the model used for the TE problem with a long wire source. The σ values are used in Eq. 64. The cross symbol and the black disks show the locations of the singular source and the observation points, respectively. The domain is composed of air and ground regions and an anomalous region located inside the ground. Middle and bottom: the starting coarse grid used for the TE model and a close-up of its center

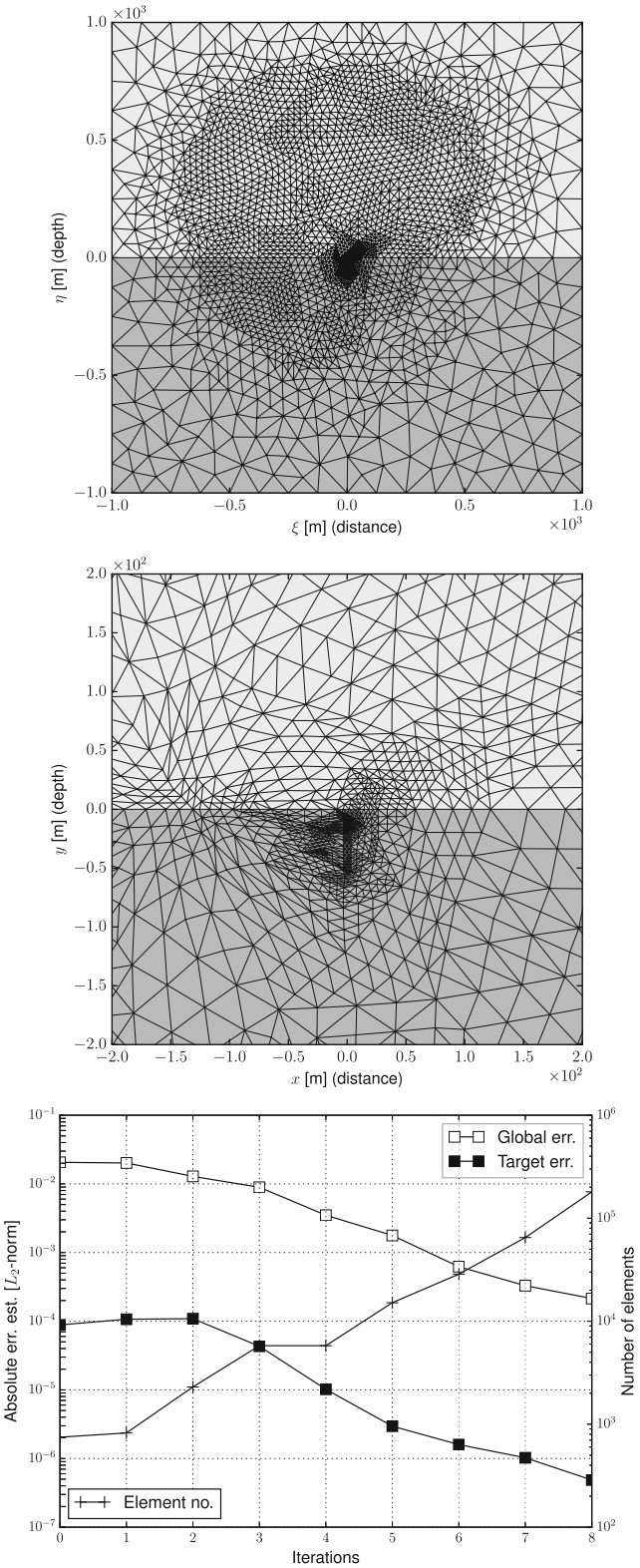

Fig. 21 A goal-oriented *hr*-adaptivity for the solution of Eq. 64, with the model in Fig. 20. Top and middle panels: the computational and physical meshes at the end of the 4th iteration, respectively. Bottom: the norm of error estimate at the target and over the entire mesh, and the number of elements for the *h*- and *r*-refinement iterations

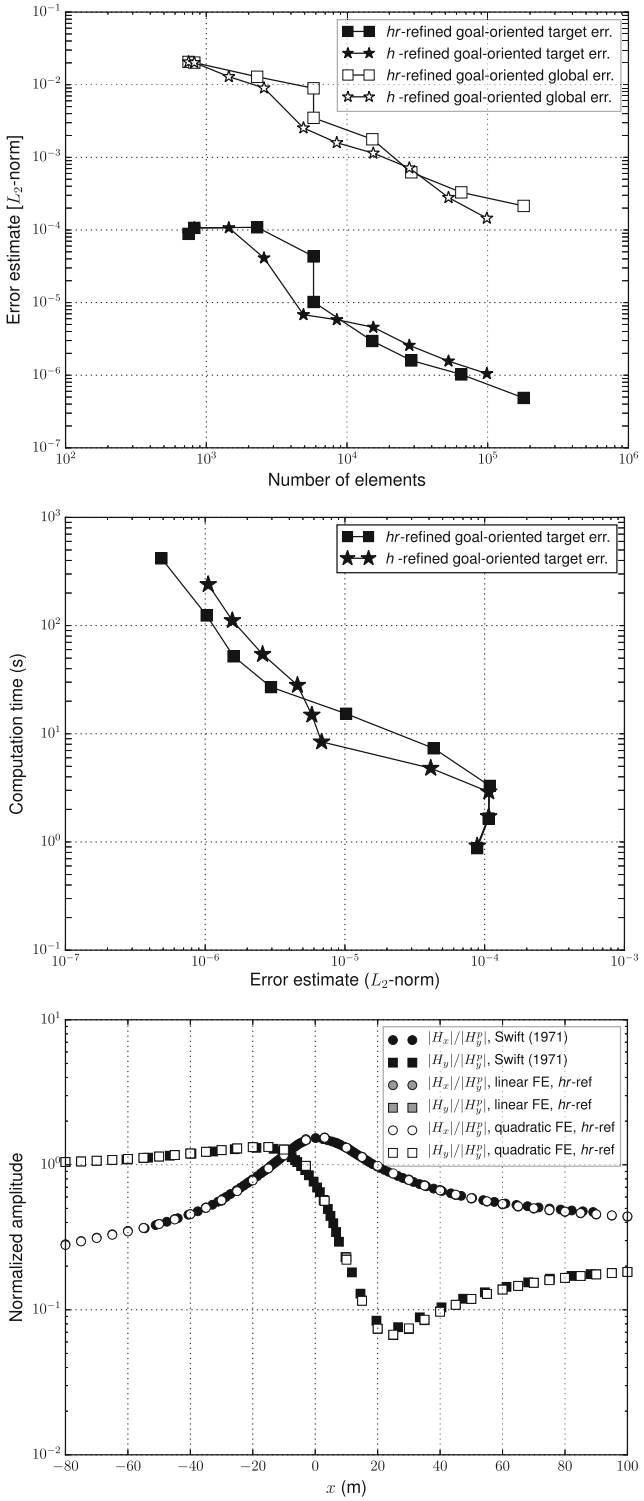

Fig. 22 The L_2-norm of error estimate over the entire mesh and at the target versus the number of elements (top) for a goal-oriented solution of Eq. 64, with the model in Fig. 20. Middle: the L_2-norm of error estimate at the target versus computation time. Results with both (pure) *h*-refinement and with *hr*-refinement are depicted. The results with *hr*-refinement correspond to the error values in the bottom panels of Fig. 21. The bottom panel gives wire response at the observation profile compared with reference data in [53]

is a certain fraction (here 50%) of the total sum of monitor function values [1, 57].

Figure 20 shows the model and the initial mesh, and example T_c and T_h grids are given at the top and middle panels of Fig. 21, respectively (the final grids are too dense to show here). The panel at the bottom of Fig. 21 gives the L_2-norm of the error estimate and the number of elements for all the *h*- and *r*-refinement iterations. Similar to the results of the previous examples, the accuracy and efficiency results in Fig. 22 show that we can reach a higher accuracy and efficiency, with the same number of elements, when we combine an *r*-refinement with the *h*-refinement. The bottom panel in Fig. 22 gives the wire response that is compared against reference data in [53]. This response is the absolute value of H_x and H_y at the observation points, normalized by the absolute value of H_y due to the free space (homogeneous wholespace).

4 Conclusions

In this study, we explore *hr*-adaptivity strategies suitable for the solution of geophysical electromagnetic (EM) modelling problem, and propose an algorithmic framework that accounts for large discontinuities in coefficients and pointwise EM observations. Motivated by the potential formulation of Maxwell's equations, one-dimensional Helmholtz and diffusion equations and a two-dimensional Helmholtz equation are considered as the physical PDEs. In 1D, a mesh PDE based on the equidistribution principle, and in 2D, mesh PDEs based on variational methods are used for the *r*-refinements. The main procedure consists of consecutive *h*- and *r*-refinements. An *r*-refinement requires the solution of the physical PDE, updating of the monitor function, and the solution of the mesh PDE, and this procedure is continued until the desired accuracy is obtained.

Using examples with a one-dimensional layered halfspace model, we conclude that fixing mesh points at the interfaces of the layers defined by the PDE coefficients and combining *h*- and *r*-refinements are both necessary for the correct equidistribution and minimization of error. It is also observed that starting the procedure with a relatively fine grid is not necessarily more efficient, in terms of the final accuracy achieved, compared to using a coarser starting mesh. Using coarse starting grids can also help to reduce the number of expensive *r*-refinement iterations (Algorithm 3 or 4) for the finer grids, which are generated by *h*-refinement, at the last iterations of the main procedure (Algorithm 1). The starting coarse grids, typically, require 3-4 *r*-refinements while the finer grids need about 2 iterations.

Two monitor functions based on hierarchical error estimates (error based and Hessian based) and one monitor

function based on a finite element residual error estimate are considered here. These monitor functions are seen to give solutions that are roughly equivalent in terms of the level of accuracy achieved with specific numbers of nodes. The rates of convergence of error with these three monitor functions are also similar. However, since hierarchical error estimates are more effective in approximating the true error, the hierarchical error–based monitor function was chosen for further experiments and combined with goal-oriented refinement. The solutions with goal-oriented error estimates show relatively higher refinement, and also improvement in accuracy, within the local regions of interest.

While 1D examples were mainly used for the derivation and testing of the algorithm, benchmark and realistic 2D examples were used for validation. These examples demonstrate the advantage of combining *h*- and *r*-refinements, compared to pure *h*-refinement, and the effectiveness of goal-oriented adaptivity, in reducing the computational effort required to reach a certain accuracy. This verifies the efficacy of the proposed algorithm for mesh adaptivity in the presence of singular sources and jumping coefficients. In a future study, we will use the proposed algorithm for practical geophysical EM modelling problems in two and three dimensions, using triangular and tetrahedral grids, respectively, leveraging recent work on efficient solution of the 3D problem [18]. Comparing *hr*-adaptivity with *hp*-refinement, and more complicated models with anisotropic media, where a different mesh generator could be required [23], may also be considered.

Acknowledgment We acknowledge the support of Research & Development Corporation Newfoundland and Labrador (RDC), and Natural Sciences and Engineering Research Council of Canada (NSERC).

References

1. Ainsworth, M., Oden, J.T.: A posteriori error estimation in finite element analysis, vol. 37. Wiley, New York (2011)
2. Alnæs, M.S., Blechta, J., Hake, J., Johansson, A., Kehlet, B., Logg, A., Richardson, C., Ring, J., Rognes, M.E., Wells, G.N.: The FEniCS project Version 1.5. Arch. Numer. Softw. **3**(100), 9–23 (2015). https://doi.org/10.11588/ans.2015.100.20553
3. Antonietti, P.F., Houston, P.: A pre-processing moving mesh method for discontinuous Galerkin approximations of advection-diffusion-reaction problems. Int. J. Numer. Anal. Model. **5**(4), 704–728 (2008)
4. Antonietti, P.F., Houston, P.: An hr-adaptive discontinuous Galerkin method for advection-diffusion problems. In: Communications to SIMAI congress, vol. 3. Open Journals Systems (2009)
5. Bank, R.E., Smith, R.K.: A posteriori error estimates based on hierarchical bases. SIAM J. Numer. Anal. **30**(4), 921–935 (1993)
6. Beckett, G., Mackenzie, J.A., Robertson, M.L.: A moving mesh finite element method for the solution of two-dimensional Stefan problems. J. Comput. Phys. **168**(2), 500–518 (2001)
7. Bihlo, A., Haynes, R.D.: Parallel stochastic methods for PDE based grid generation. Comput. Math. Appl. **68**(8), 804–820 (2014)
8. Biswas, R., Flaherty, J.E., Arney, D.C.: An adaptive mesh-moving and refinement procedure for one-dimensional conservation laws. Appl. Numer. Math. **11**(4), 259–282 (1993)
9. Brenner, S.C., Scott, L.R.: The mathematical theory of finite element methods, vol. 15. Springer, Berlin (2008)
10. Budd, C.J., Huang, W., Russell, R.D.: Adaptivity with moving grids. Acta Numer. **18**, 111–241 (2009)
11. Cao, W., Huang, W., Russell, R.D.: An *r*-adaptive finite element method based upon moving mesh PDEs. J. Comput. Phys. **149**(2), 221–244 (1999)
12. Cao, W., Huang, W., Russell, R.D.: A study of monitor functions for two-dimensional adaptive mesh generation. SIAM J. Sci. Comput. **20**(6), 1978–1994 (1999)
13. Ceniceros, H.D., Hou, T.Y.: An efficient dynamically adaptive mesh for potentially singular solutions. J. Comput. Phys. **172**(2), 609–639 (2001)
14. Chave, A.D., Jones, A.G. (eds.): The magnetotelluric method: theory and practice. Cambridge University Press, Cambridge (2012)
15. Demkowicz, L.: Computing with hp-adaptive finite elements: volume 1. One and two dimensional elliptic and Maxwell problems. Chapman and Hall/CRC (2006)
16. Druskin, V., Knizhnerman, L., Lee, P.: A new spectral Lanczos decomposition method for induction modeling in arbitrary 3-d geometry. Geophysics **64**, 701–706 (1999)
17. Edwards, M.G., Oden, J.T., Demkowicz, L.: An hr-adaptive approximate Riemann solver for the Euler equations in two dimensions. SIAM J. Sci. Comput. **14**(1), 185–217 (1993)
18. Grayver, A.V., Kolev, T.V.: Large-scale 3D geoelectromagnetic modeling using parallel adaptive high-order finite element method. Geophysics **80**(6), E277–E291 (2015)
19. Griffiths, D.J. Introduction to Electrodynamics, 3rd edn. Prentice-Hall Inc., New Jersey (1999)
20. Hagmeijer, R.: Grid adaption based on modified anisotropic diffusion equations formulated in the parametric domain. J. Comput. Phys. **115**(1), 169–183 (1994)
21. He, Y., Huang, W.: A posteriori error analysis for finite element solution of one-dimensional elliptic differential equations using equidistributing meshes. J. Comput. Appl. Math. **299**, 101–126 (2016)
22. Huang, W.: Practical aspects of formulation and solution of moving mesh partial differential equations. J. Comput. Phys. **171**(2), 753–775 (2001)
23. Huang, W., Kamenski, L., Lang, J.: A new anisotropic mesh adaptation method based upon hierarchical a posteriori error estimates. J. Comput. Phys. **229**(6), 2179–2198 (2010)
24. Huang, W., Russell, R.D.: A high dimensional moving mesh strategy. Appl. Numer. Math. **26**(1-2), 63–76 (1998)
25. Huang, W., Russell, R.D.: Moving mesh strategy based on a gradient flow equation for two-dimensional problems. SIAM J. Sci. Comput. **20**(3), 998–1015 (1998)
26. Huang, W., Russell, R.D.: Adaptive moving mesh methods, vol. 174. Springer Science & Business Media, Berlin (2010)
27. Huang, W., Sun, W.: Variational mesh adaptation II: error estimates and monitor functions. J. Comput. Phys. **184**(2), 619–648 (2003)
28. Jahandari, H., Farquharson, C.G.: A finite-volume solution to the geophysical electromagnetic forward problem using unstructured grids. Geophysics **79**(6), E287–E302 (2014)

29. Jahandari, H., Farquharson, C.G.: Finite-volume modelling of geophysical electromagnetic data on unstructured grids using potentials. Geophys. J. Int. **202**, 1859–1876 (2015)
30. Johnson, C.: Numerical solution of partial differential equations by the finite element method. Courier Corporation (2012)
31. Kamenski, L.: A study on using hierarchical basis error estimates in anisotropic mesh adaptation for the finite element method. Eng. Comput. **28**(4), 451–460 (2012)
32. Key, K., Ovall, J.: A parallel goal-oriented adaptive finite element method for 2.5-D electromagnetic modelling. Geophys. J. Int. **186**, 137–154 (2011)
33. Key, K., Weiss, C.: Adaptive finite-element modeling using unstructured grids: the 2D magnetotelluric example. Geophysics **71**, G291–G299 (2006)
34. Lang, J., Cao, W., Huang, W., Russell, R.D.: A two-dimensional moving finite element method with local refinement based on a posteriori error estimates. Appl. Numer. Math. **46**(1), 75–94 (2003)
35. Li, R., Tang, T., Zhang, P.: Moving mesh methods in multiple dimensions based on harmonic maps. J. Comput. Phys. **170**(2), 562–588 (2001)
36. Li, Y., Key, K.: 2D marine controlled-source electromagnetic modeling: part 1 - an adaptive finite element algorithm. Geophysics **72**(2), WA51–WA62 (2007)
37. Li, Y., Pek, J.: Adaptive finite element modelling of two-dimensional magnetotelluric fields in general anisotropic media. Geophys. J. Int. **175**(3), 942–954 (2008)
38. Liu, Y., Xu, Z., Li, Y.: Adaptive finite element modelling of three-dimensional magnetotelluric fields in general anisotropic media. J. Appl. Geophys. **151**, 113–124 (2018)
39. Logg, A., Wells, G.N., Hake, J.: DOLFIN: A C++/python finite element library. In: Logg, A., Mardal, K.A., Wells, G.N. (eds.) Automated solution of differential equations by the finite element method, Volume 84 of lecture notes in computational science and engineering, chap. 10. Springer (2012)
40. Materna, D., Barthold, F.J.: Configurational variations for the primal and dual problem in elasticity. ZAMM J. Appl. Math. Mech. **89**(8), 666–676 (2009)
41. Materna, D., Barthold, F.J.: Goal-oriented r-adaptivity based on variational arguments in the physical and material spaces. Comput. Methods Appl. Mech. Eng. **198**(41-44), 3335–3351 (2009)
42. Mitsuhata, Y., Uchida, T.: 3D magnetotelluric modeling using the T-Ω finite-element method. Geophysics **69**(1), 108–119 (2004)
43. Newman, G.A., Alumbaugh, D.L.: Frequency-domain modeling of airborne electromagnetic responses using staggered finite differences. Geophys. Prospect. **43**, 1021–1042 (1995)
44. Newman, G.A., Alumbaugh, D.L.: Three-dimensional induction logging problems, part 2: a finite-difference solution. Geophysics **67**(2), 484–491 (2002)
45. Oden, J.T., Prudhomme, S.: Goal-oriented error estimation and adaptivity for the finite element method. Comput. Math. Appl. **41**(5-6), 735–756 (2001)
46. Ong, B., Russell, R., Ruuth, S.: An h-r moving mesh method for one-dimensional time-dependent PDEs. In: Proceedings of the 21st international meshing roundtable, pp. 39–54. Springer (2013)
47. Ovall, J.S.: Asymptotically exact functional error estimators based on superconvergent gradient recovery. Numer. Math. **102**(3), 543–558 (2006)
48. Pardo, D., Demkowicz, L., Torres-Verdin, C., Paszynski, M.: A self-adaptive goal-oriented hp-finite element method with electromagnetic applications. Part II: electrodynamics. Comput. Methods Appl. Mech. Eng. **196**(37-40), 3585–3597 (2007)
49. Rannacher, R., Suttmeier, F.T.: A posteriori error control in finite element methods via duality techniques: application to perfect plasticity. Comput. Mech. **21**(2), 123–133 (1998)
50. Ren, Z., Kalscheuer, T., Greenhalgh, S., Maurer, H.: A goal-oriented adaptive finite-element approach for plane wave 3-D electromagnetic modelling. Geophys. J. Int. **194**, 700–718 (2013)
51. Schwab, C.: *p*- and hp-finite element methods: theory and applications in solid and fluid mechanics. Oxford University Press, Oxford (1998)
52. Schwarzbach, C., Börner, R.U., Spitzer, K.: Three-dimensional adaptive higher order finite element simulation for geo-electromagnetics–a marine CSEM example. Geophys. J. Int. **187**, 63–74 (2011)
53. Swift, C.M. Jr.: Theoretical magnetotelluric and Turam response from two-dimensional inhomogeneities. Geophysics **36**(1), 38–52 (1971)
54. Szabó, B.A., Babuška, I.: Finite element analysis. Wiley, New York (1991)
55. Tan, Z., Huang, Y.: An alternating Crank-Nicolson method for the numerical solution of the phase-field equations using adaptive moving meshes. Int. J. Numer. Methods Fluids **56**(9), 1673–1693 (2008)
56. Tang, T.: Moving mesh methods for computational fluid dynamics. Contemp. Math. **383**, 141–174 (2005)
57. Verfürth, R.: A posteriori error estimation techniques for finite element methods. OUP Oxford (2013)
58. Wang, D., Wang, X.P.: A three-dimensional adaptive method based on the iterative grid redistribution. J. Comput. Phys. **199**(2), 423–436 (2004)
59. Ward, S.M., Hohmann, G.W.: Electromagnetic theory for geophysical applications. In: Nabighian, M.N. (ed.) Electromagnetic methods in applied geophysics, vol. 1, Theory, pp. 131–308. Society of Exploration Geophysicists (1988)
60. Winslow, A.M.: Numerical solution of the quasilinear Poisson equation in a nonuniform triangle mesh. J. Comput. Phys. **1**(2), 149–172 (1966)
61. Winslow, A.M.: Adaptive-mesh zoning by the equipotential method. Tech. rep., Lawrence Livermore National Lab., CA (USA) (1981)
62. Zegeling, P.A.Tang, T., Xu, J. (eds.): Theory and application of adaptive moving grid methods. Science Press, Beijing (2007)
63. Zhang, Z., Naga, A.: A new finite element gradient recovery method: superconvergence property. SIAM J. Sci. Comput. **26**(4), 1192–1213 (2005)
64. Zienkiewicz, O.C., Zhu, J.Z.: The superconvergent patch recovery and a posteriori error estimates. Part 1: the recovery technique. Int. J. Numer. Methods Eng. **33**(7), 1331–1364 (1992)
65. Zienkiewicz, O.C., Zhu, J.Z.: The superconvergent patch recovery and a posteriori error estimates. Part 2: error estimates and adaptivity. Int. J. Numer. Methods Eng. **33**(7), 1365–1382 (1992)

Affiliations

Hormoz Jahandari[1] · Scott MacLachlan[1] · Ronald D. Haynes[1] · Niall Madden[2]

Scott MacLachlan
smaclachlan@mun.ca

Ronald D. Haynes
rhaynes@mun.ca

Niall Madden
Niall.Madden@NUIGalway.ie

[1] Department of Mathematics and Statistics, Memorial University of Newfoundland, St. John's, NF, Canada

[2] School of Mathematics, Statistics and Applied Mathematics, National University of Ireland Galway, Galway, Ireland